ISSN 1331-7210

Engineering Power

BULLETIN OF THE CROATIAN ACADEMY OF ENGINEERING Vol. 17(4) 2022

EDITOR-IN-CHIEF'S WORD

Dear Readers,

The Croatian Academy of Engineering devotes great care to the publication of our regular issues, which cover a wide range of interesting topics. In our latest issue of Engineering Power, we are devoted to two interesting areas: inorganic chemical technology and metallurgy. With this issue, we aim to provide our readers with valuable insights into these fascinating fields. By addressing inorganic chemical technology and metallurgy, we aim to shed light on their importance and the ongoing advances that are shaping modern engineering practice. This endeavor is consistent with our important goal of reindustrializing the country, and we hope to demonstrate the transformative potential of these disciplines.

Editor-in-Chief
Vedran Mornar, President of the Croatian Academy of Engineering

EDITOR'S WORD

Dear readers,

It is my great pleasure to present the issue of Engineering Power edited by Prof. Stanislav Kurajica, Ph.D. In the four articles in this issue, he has succeeded in presenting the most important scientific research activities of the Department of Inorganic Chemical Technology and Nonmetals of the University of Zagreb, Faculty of Chemical Engineering and Technology. Bioactive glass composite, ceria nanoparticles catalyst, thin films for energy conversion, and acoustic cement are the scientific topics covered in this issue. Enjoy reading!

Editor
Bruno Zelić, Vice-President of the Croatian Academy of Engineering

FOREWORD

Dear readers,

The Department of Inorganic Chemical Technology and Metallurgy of the Chemical Engineering Institute of the Higher technical school was founded in 1922. Over time, the Department operates as part of the Faculty of Engineering, the Faculty of Technology and finally the Faculty of Chemical Engineering and Technology of the University of Zagreb. The Department has been dealing with materials since the very beginning, eventually becoming internationally recognizable in the areas of glass, ceramics and mineral binders. Accordingly, it changed its name to the Department of Inorganic Chemical Technology and Nonmetals. At the beginning of millennium, the Department turned to nanotechnology and new materials, and if it ever changes its name again, according to the area of scientific, teaching and professional work, the name Department for Advanced Materials and Nanotechnology would suit it best. The Department continues to be characterized by intense scientific activity, competitive projects and publications in esteemed journals. In 2022, five professors, two senior assistants, two postdoctoral students, one assistant and seven doctoral students worked at the Department. During that year, one PZS, four HRZZ projects, three IRI projects and four bilateral projects were carried out at the Department, also four financial grants for research from the University of Zagreb were received. Again, during that year, 29 scientific papers were published in journals cited in the CC database, as well as numerous other scientific papers. Four scientific groups can be clearly distinguished in the Department; my intention was to present their work through topics of their choice. Although each of the groups has several areas of research in which they have top competences, to my satisfaction, they chose the topics on which they are currently most active. Thus, papers on bioactive glass composite, ceria nanoparticles catalyst, thin films for energy conversion, and acoustic cement boards are included. I hope you find some of these topics close to your own interests.

Guest-Editor
Stanislav Kurajica, University of Zagreb, Faculty of Chemical Engineering and Technology

CONTENT

Andrea Lončarević, Leonard Bauer, Anamarija Rogina, Hrvoje Ivanković

Preparation of chitosan-copper complex microspheres modified by bioactive glass

Faculty of Chemical Engineering and Technology University of Zagreb, Trg Marka Marulića 19, HR-10000 Zagreb Croatia

Abstract

The aim of this work was to prepare composite microspheres with high sphericity and narrow size distribution based on chitosan-copper complex and bioactive glass (bioglass). The influence of the bioactive glass content on the size and morphology of chitosan-copper complex microspheres was investigated. The electrohydrodynamic atomization process was used to produce highly spherical particles of narrow size distribution and with defined surface morphology. The addition of bioglass particles caused the surface changes, from smooth to wrinkled surface by increasing the bioglass quantity. The size of the obtained microspheres was estimated to be between 40 and 100 μm, depending on the bioglass content.

***Keywords**: chitosan, bioactive glass, electrospraying, microspheres*

1. Introduction

Natural human bone undergoes continuous process of formation, resorption and remodeling. In small defects of damage, bone possesses the self-healing ability [1]. However, larger defects which usually originate from surgical resection require implants, i.e., temporary supports for cell adhesion, proliferation and tissue regeneration. Furthermore, sufficient vascularization is necessary for the repair of the large bone defects, providing transports of oxygen, nutrients and osteoprogenitor cells to facilitate bone regeneration [2]. Bioactive glasses (bioglass, BG) are recognized as promising biomaterials in bone repair application due to their bioactivity, pro-osteogenic and pro-angiogenic abilities [3]. On the other hand, chitosan-based microspheres have been exploited as carriers of bioactive molecules due to the targeted delivery [4,5]. More significantly, polycationic nature of chitosan allows it to interact with metal ions involved in biological processes of bone formation and remodeling, called therapeutic metal ions (TMIs) [6].

The application of therapeutic metal ions emerges as a potential alternative for tissue regeneration without using expensive biomolecules, such as growth factors [7]. Copper, zinc, magnesium and strontium belong to a family of therapeutic metal ions due to their key role in regulating physiological pathways, such as angiogenesis, osteogenesis, proliferation, differentiation, and antibacterial properties. Combining biologically active ions with pH-responsive chitosan microspheres and bioactive glasses could generate multifunctional carriers and delivery systems for bone tissue engineering. The physical nature of complexation interactions of chitosan and doped BGs can optimize the delivery of necessary therapeutic metal ions, which play an important role during angiogenesis and homeostasis.

This work proposes the production of microsized biodegradable matrices functionalized by copper (II) ions through complexation reactions with chitosan and their modification by bioactive glasses. The electrohydrodynamic atomization process was used to produce microspheres with a narrow size distribution. Furthermore, the different content of bioglass affected the morphology and size of the microspheres.

2. Experimental part

2.1. Materials

In this work, Chitosan with DD = 87% (Chitoscience, CHT85/100) was purchased from Heppe Medical Chitosan GmbH (Halle (Saale), Germany). Copper acetate monohydrate (BDH Prolabo, Leuven, Belgium) was used as a precursor of copper (II) ions (Cu^{2+}) for the complexes' preparation. Other chemicals for materials preparation were 99.8% acetic acid (HAc; Lach–Ner, Neratovice, Czech Republic), sodium hydroxide (NaOH; Honeywell, Seelze, Germany), 96% ethanol (EtOH; Kefo, Ljubljana, Slovenia) and acetone (T.T.T. doo, Sveta Nedjelja, Croatia). All chemicals were of analytic grade. Bioactive glass powder (45S5 [8], particle size ~4 μm) was kindly provided by Prof. A.R. Boccaccini for the preparation of composite microspheres.

2.2. Preparation of chitosan-Cu/BG solutions

1.0 wt.% chitosan solution was prepared by dissolving polymer powder in 1% solution of acetic acid for 2 h at ambient conditions.

The chitosan–copper (II) ions complex solutions were prepared by mixing the appropriate weight of copper acetate monohydrate into 1.0 wt% chitosan solution followed by stirring for 2 h. The prepared CHT–copper (II) solution was designated as CHT–Cu3. As described in detail in our previous work [9], the amount of Cu^{2+} ions was added with respect to the molar ratio of Cu^{2+} ions and amino groups in chitosan as $n(Cu^{2+}) : n(-NH_2) = 0.0549:1$.

The chitosan-Cu solutions modified by bioglass particles (CHT-Cu/BG) were prepared by mixing the CHT-Cu3 solution with the 1, 2, 3, 4, 5 and 10 wt.% of bioglass and were designated as CHT-Cu/1BG, CHT-Cu/2BG, CHT-Cu/3BG, CHT-Cu/4BG, CHT-Cu/5BG and CHT-Cu/10BG, respectively. Furthermore, 5 wt.% sodium hydroxide solution (NaOH) was used as a gelation medium during the electrohydrodynamic atomization process. All solutions were freshly prepared for each microsphere production.

2.3. Chitosan-Cu/BG microsphere production

The electrospraying process was performed using the setup shown in Figure 1, applying the constant process parameters given in Table 1.

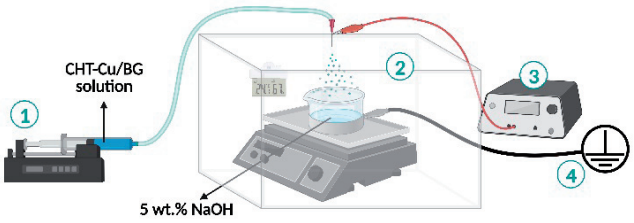

Fig. 1. Schematic illustration of electrospraying setup. 1 - syringe pump; 2 - isolating chamber; 3 - high voltage generator; 4 - grounding. Created with BioRender.com.

Table 1. Parameters of electrospraying process.

Parameter	Unit	Value
Concentration of acetic acid	%	1.0
Initial concentration of chitosan solution	wt.%	1.0
Flow rate of solution	mL h^{-1}	5
Needle gauge	G	23
Applied voltage	kV	20
Distance between the needle tip and collector	cm	10
Concentration of NaOH	wt.%	5
Volume of NaOH (collector)	mL	50
Duration of electrospraying	min	60
Temperature (in the chamber)	°C	25 ± 1
Relative humidity (in the chamber)	%	66 ± 5

The electrospraying process was conducted as follows: the syringe (Becton Dickinson, Le Pont-de-Claix, France) was filled with the prepared chitosan–Cu complex solution (10 mL) and processing parameters presented in Table 1 were set. The needle was positively charged, and the collector was grounded. The container with 50 mL of gelation medium isolated with aluminum foil was used as the collector. The distance between the collector and the blunt tip needle was 10 cm. The required voltage for the electrospraying process was determined according to the formation of stable Taylor cone-jet mode. For CHT85/100-Cu3/BG-based complex solutions, a stable jet was observed at the voltage of 20 kV. The flow rate of solutions was 5 mL h^{-1} and the process was performed for 60 min without interruption, while gentle stirring the gelation medium.

After electrospraying, the gelation medium containing produced microspheres was stored for the next 2 h to complete gelation. Microspheres were then washed with distilled water until neutral pH, dehydrated with 96% EtOH for 2 h and acetone for several times. At the end, microspheres were left at the ambient conditions for solvent evaporation.

2.4. Characterization of chitosan-Cu/BG microspheres

The composite microspheres were analyzed with a BA200 binocular microscope (light microscope; Motic Instruments, Barcelona, Spain). Pictures were taken using the Motic Images Plus 2.0 program and processed by ImageJ 1.53e software used for the estimation of the microspheres' size. The diameter was calculated from the area of at least 100 randomly chosen microspheres, assuming the total sphericity of microspheres.

The morphology of composite microspheres was investigated by scanning electron microscopy (SEM; Tescan Vega III Easyprobe, Brno-Kohoutovice, Czech Republic) with an electron beam energy of 10 keV. Prior to imaging, microspheres were sputtered with gold and palladium for 60 s.

3. Results and discussion

The functionalization of chitosan with divalent metal ions can be accomplished by simple complexation chemistry, where amino, amide and hydroxyl groups of chitosan act as ligands in metal coordination. Such physical interactions can improve mechanical properties of chitosan [10]. Previously [11], we prepared copper (II)-chitosan complex microspheres, where Cu–chitosan complexes with higher Cu^{2+} amount showed more stable microspheres produced by electrospraying. Moreover, FTIR spectroscopy indicated structural changes of chitosan where free hydroxyl and amino groups are involved in metal coordination. Such coordination can form structures that can be described by two models, 'pendant' and 'bridge' model [12]. Several types of $[CuNH^2(OH)^2X]$ complexes (where X can be water molecules or hydroxyl groups of chitosan) with 'pendant' configuration were proposed [13]. Depending on the pH of aqueous solution, copper can be

coordinated by amino group, hydroxide ions and water molecules. On the contrary, the 'bridge' model was described by the tetrahedral coordination with amino groups of the same or a different chitosan chain.

In the present study, the previously developed chitosan-copper complex microspheres were modified by bioactive glass particles to extend their functionality for bone tissue engineering application. The successful production of bioglass-modified microspheres was observed using optical microscope, shown in Figure 2. The produced composite microspheres were spherical regardless of the bioglass content. In our previous work [11], we showed that the concentration of copper (II) ions influences the production of spherical particles. Chitosan-Cu complex systems with lower $c(Cu^{2+})$ yielded deformed particles or precipitates of an undefined shape as a result of less physical crosslinks between amino and hydroxyl group and metal ion. Taking into account good sphericity of composite microparticles, we could assume that the addition of BG particles did not significantly affect the physical crosslink between chitosan and copper (II) ions.

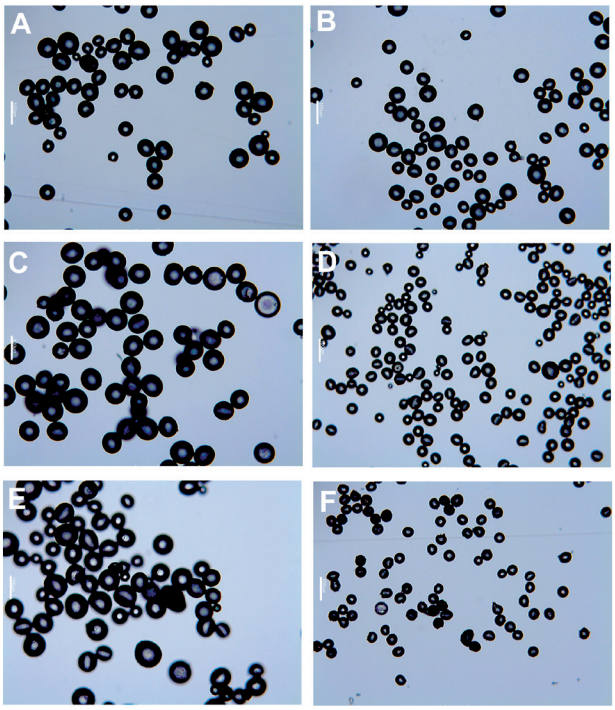

Fig. 2. Chitosan-copper complex microspheres with different amount of BG particles: A) 1%, B) 2%, C) 3%, D) 4%, E) 5%, F) 10%. Scale bar: 100 µm.

The size distribution of composite microspheres was estimated by light microscopy (Figure 3).

The size of composite microspheres ranged from 60 to 100 µm, depending on the BG content. The addition of bioglass particles had an impact on the distribution of particles size, i.e. the composite microspheres with 10% of BG showed the narrowest size distribution. Furthermore, the highest amount of BG particles resulted in the smallest composite microspheres (size of 40 – 60 µm).

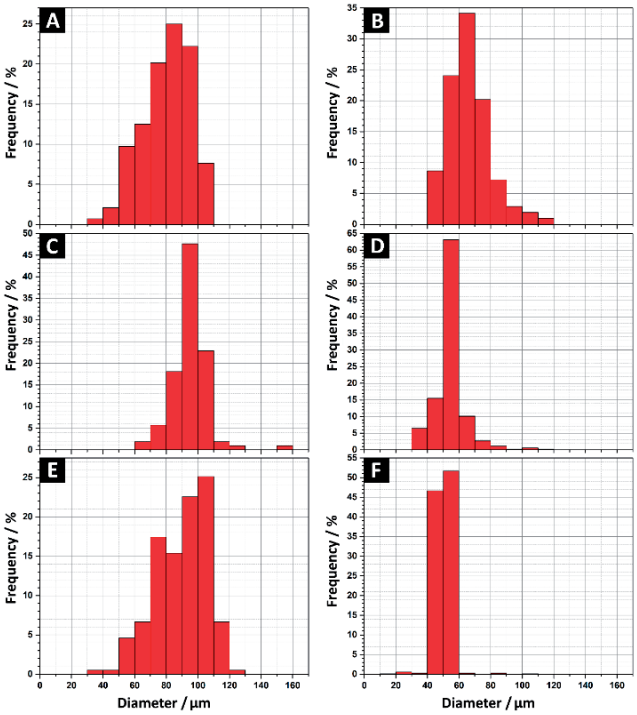

Fig. 3. Size distribution of A) CHT-Cu/1BG, B) CHT-Cu/2BG, C) CHT-Cu/3BG, D) CHT-Cu/4BG, E) CHT-Cu/5BG and F) CHT-Cu/10BG microspheres.

The viscosity and surface tension of the polymer solution are the main parameters that influence the electrospraying process [14]. A previous study indicated that larger particles are obtained when a higher viscosity of solution is applied [15]. For our chitosan-Cu complex solutions [11], the viscosity was decreased by a higher Cu concentration as a result of the complex formation. Here, a possible reason for obtaining smaller particles of the composite with 10% of BG could be changes in viscosity caused by physical interactions between polymer macromolecules and BG particles.

The influence of BG particles on microsphere morphology was observed in SEM micrographs (Figure 4). Gradual surface changes were observed with an increase of the BG content.

Microspheres with 1% of BG particles showed a smoother surface, while 10% of BG resulted in a non-homogeneous surface with noticeable wrinkling. Furthermore, some microspheres were slightly deformed. During the electrohydrodynamic atomization process, the applied electric field needs to overcome the surface tension of the polymeric solution to generate a drop. It has been observed [16] that a stronger field is required for a higher surface tension in order to obtain the regular shape of the microsphere. In the present study, all composite systems were produced at constant voltage, where only composite 10% BG yielded microspheres with different shape. It can be assumed that a higher addition of BG particles significantly changes the surface tension of the chitosan-Cu solution which in the end influences the microsphere shape and morphology. However, this effect needs to be confirmed by further in-

vestigation including electrospraying performed at different processing parameters.

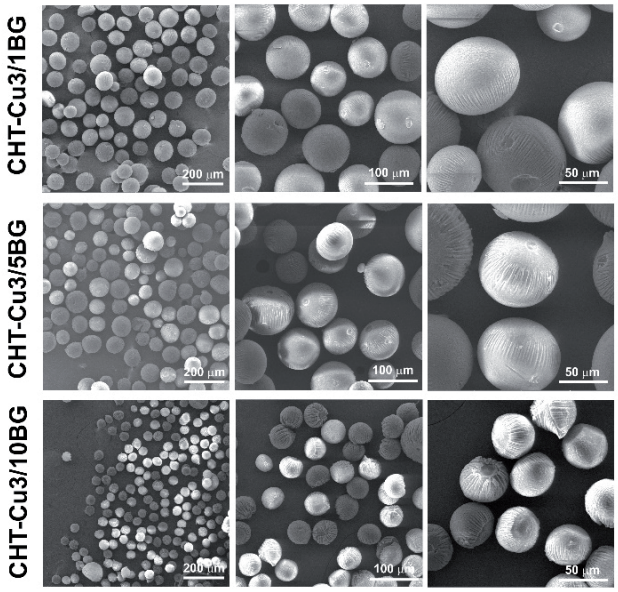

Fig. 4. SEM micrographs of chitosan-copper complex microspheres with 1%, 5% and 10% of BG microparticles at different magnification.

4. Conclusion

The electrohydrodynamic atomization process was used to produce chitosan-copper (II) microspheres modified by bioactive glass microparticles in this research. The increase of bioglass amount resulted in smaller microspheres with a narrow size distribution. Furthermore, microspheres containing 10% bioglass had greater surface roughness and minor shape deformation. The electrohydrodynamic atomization process could be a promising method for producing chitosan-Cu microspheres modified by inorganic phase.

5. References

[1] R. Dimitriou, E. Jones, D. McGonagle, P. V. Giannoudis, Bone regeneration: Current concepts and future directions, BMC Med. 9 (2011) 1–10.

[2] W. Yu, T.-W.W. Sun, Z. Ding, C. Qi, H. Zhao, F. Chen, Z. Shi, Y.-J.J. Zhu, D. Chen, Y. He, Copper-doped mesoporous hydroxyapatite microspheres synthesized by a microwave-hydrothermal method using creatine phosphate as an organic phosphorus source: application in drug delivery and enhanced bone regeneration, J. Mater. Chem. B. 5 (2017) 1039–1052.

[3] H. Sun, K. Zheng, T. Zhou, A.R. Boccaccini, Incorporation of Zinc into Binary SiO2-CaO Mesoporous Bioactive Glass Nanoparticles Enhances Anti-Inflammatory and Osteogenic Activities, Pharm. 13 (2021) 2124.

[4] Y. Zhou, H.-L. Gao, L.-L. Shen, Z. Pan, L.-B. Mao, T. Wu, J.-C. He, D.-H. Zou, Z.-Y. Zhang, S.-H. Yu, Chitosan microspheres with an extracellular matrix-mimicking nanofibrous structure as cell-carrier building blocks for bottom-up cartilage tissue engineering, Nanoscale. 8 (2016) 309–317.

[5] M.A. Islam, J. Firdous, Y.J. Choi, C.H. Yun, C.S. Cho, Design and application of chitosan microspheres as oral and nasal vaccine carriers: An updated review, Int. J. Nanomedicine. 7 (2012) 6077–6093.

[6] M. Rhazi, J. Desbrières, A. Tolaimate, M. Rinaudo, P. Vottero, A. Alagui, M. El Meray, Influence of the nature of the metal ions on the complexation with chitosan.: Application to the treatment of liquid waste, Eur. Polym. J. 38 (2002) 1523–1530.

[7] V. Mouriño, J.P. Cattalini, A.R. Boccaccini, Metallic ions as therapeutic agents in tissue engineering scaffolds: an overview of their biological applications and strategies for new developments, J. R. Soc. Interface. 9 (2012) 401–419.

[8] M.L. Dittler, P.M. Zelís, A.M. Beltrán, R. Destch, C.A. Grillo, M.C. Gonzalez, A.R. Boccaccini, Magnetic 3D scaffolds for tissue engineering applications: bioactive glass (45S5) coated with iron-loaded hydroxyapatite nanoparticles, Biomed. Mater. 16 (2021) 055006.

[9] A. Rogina, A. Lončarević, M. Antunović, I. Marijanović, M. Ivanković, H. Ivanković, Tuning physicochemical and biological properties of chitosan through complexation with transition metal ions, Int. J. Biol. Macromol. 129 (2019) 645–652.

[10] J. Nie, Z. Wang, Q. Hu, Chitosan Hydrogel Structure Modulated by Metal Ions, Sci. Rep. 6 (2016) 1–8.

[11] A. Lončarević, M. Ivanković, A. Rogina, Electrosprayed chitosan–copper complex microspheres with uniform size, Materials (Basel). 14 (2021) 5630.

[12] K. Ogawa, K. Oka, T. Yui, X-ray Study of Chitosan-Transition Metal Complexes, Chem. Mater. 5 (1993) 726–728.

[13] M. Rhazi, A. Tolaimate, M. Rhazi, J. Desbriéres, A. Tolaimate, M. Rinaudo, A. Alagui, P. Vottero, Contribution to the study of the complexation of copper by chitosan and oligomers, Polymer 43 (2001) 1267–1276.

[14] J.A. Tapia-Hernández, P.I. Torres-Chávez, B. Ramírez-Wong, A. Rascón-Chu, M. Plascencia-Jatomea, C.G. Barreras-Urbina, N.A. Rangel-Vázquez, F. Rodríguez-Félix, Micro- and Nanoparticles by Electrospray: Advances and Applications in Foods, J. Agric. Food Chem. 63 (2015) 4699–4707..

[15] N. Ardila, Z. Ajji, M.C. Heuzey, A. Ajji, Chitosan electrospraying: Mapping of process stability and micro and nanoparticle formation, J. Aerosol Sci. 126 (2018) 85–98.

[16] A. Bateni, A. Ababneh, J.A.W. Elliott, A.W. Neumann, A. Amirfazli, Effect of gravity and electric field on shape and surface tension of drops, in: Adv. Sp. Res. (2005) 64–69.

Katarina Mužina, Ivana Katarina Ivković, Stanislav Kurajica

Electrochemical and catalytic applications of cerium(IV) oxide

University of Zagreb, Faculty of Chemical Engineering and Technology, Marulićev trg 19, HR 10000, Zagreb, Croatia

Abstract

Cerium(IV) oxide is one of the most important rare earth metal oxides owing to its high oxygen storage and release capacity, as well as thermal and mechanical stability. Its various applications range from sensors, solid oxide fuel cells and supercapacitors to the most important catalytic application in three-way catalytic converters, oxidation of volatile organic molecules, water-gas shift reaction, etc. This short review article gives a brief introduction to rare earth metals, then describes in detail the properties of cerium(IV) oxide and ways to improve them, as well as presents an overview of the most important and current applications of cerium(IV) oxide. Finally, it gives an overview of the results obtained by our group regarding pure and doped cerium(IV) oxide for various applications.

***Keywords**: cerium(IV) oxide, doping, nanotechnology, catalysis.*

1. Introduction

Rare earth elements are a group of 17 chemically similar elements and include lanthanides, scandium and yttrium. They are all silver, silvery-white, or grey lustrous metals and are usually divided into light (from lanthanum to gadolinium) and heavy (from terbium to lutetium and yttrium), depending on the electronic configuration, which influences their respective properties. Although the name suggests the opposite, rare earth metals are relatively well distributed in the Earth's crust, but very rarely concentrated in recoverable ore deposits. Due to the similarities in structure, they naturally appear together in minerals and are found with non-metals, especially strong electronegative elements such as oxygen or fluorine. Rare earth metals and their compounds are widely used in various industries, and are thus used in metallurgy, glass and ceramic polishing, for the production of electronic components, as permanent magnets, and as catalysts in technological chemical processes, the automotive industry and petroleum refining. [1, 2] The most abundant of rare earth elements is cerium, which has two stable oxidation states, Ce^{3+} and Ce^{4+}, and can therefore form two types of oxides, Ce_2O_3 and CeO_2. Cerium (IV) oxide possesses a higher application value and has therefore been the subject of considerable research in recent years. [3, 4]

2. Cerium(IV) oxide

Cerium(IV) oxide or ceria (CeO_2) has a fluorite type crystal structure with space group Fm3m in which ceria cations form the face centered cubic cell, while the oxygen anions occupy the tetrahedral interstices (Figure 1). Each cerium cation is coordinated by eight neighboring oxygen anions and each oxygen anion is coordinated by four neighboring cerium cations. This structure is stable over the whole temperature range from room temperature until the melting point. [5]

Pure stoichiometric ceria has a pale yellow color, which is assumed to be due to Ce(IV)-O(-II) charge transfer. [5] As already mentioned, cerium can be chemically present in two stable valence states, Ce (IV) and Ce (III), and the special feature of ceria fluorite lattice is that it can tolerate a considerable reduction of Ce^{4+} to Ce^{3+} (Eq. 1) without any structural changes, particularly at high temperatures.

$$Ce^{4+} + e^- \leftrightarrows Ce^{3+} \qquad \text{(Eq. 1)}$$

Such nonstoichiometric ceria CeO^2-δ ($0 < \delta < 0.5$) has blue color and can even turn black when largely nonstoichiometric. [4, 5]

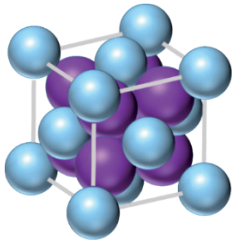

Figure 1. Ceria unit cell: Cerium cations (blue spheres) form a plane-centered cubic lattice, while oxygen anions (magenta spheres) occupy tetrahedral interstices.

When CeO_2 is further reduced, it forms the hexagonal cerium sesquioxide Ce_2O_3 with a P3m1 space group. As a result of the ease with which Ce^{4+} may be reduced to Ce^{3+}, oxygen is released as a compensatory effect, resulting in mixed ionic electronic conductivity (MIEC) of ceria (Eq. 2). [6, 7]

$$CeO_2 \leftrightarrows CeO_{2-\delta} + \frac{\delta}{2} O_2 \qquad \text{(Eq. 2)}$$

In the course of this process oxygen vacancies are formed in the crystal lattice. The Ce^{3+} can easily be reoxidized by oxygen uptake, which makes ceria a suitable material for redox related catalytic applications or oxygen buffers. [7, 9] Good catalytic activity of CeO_2 can mostly be attributed to the easy shift between Ce^{3+} and Ce^{4+} oxidation

states, creation of oxygen vacancies and thereby high oxygen mobility and oxygen storage capacity (OSC) within the ceria crystal lattice. [5, 6]

Oxygen vacancies defects are prone to change depending on physical parameters such as temperature, oxygen partial pressure, doping of ceria with foreign ions, electrical field or surface stresses. Nevertheless, oxygen vacancies are the most important feature of ceria and they greatly influence its electronic and chemical properties. [6]

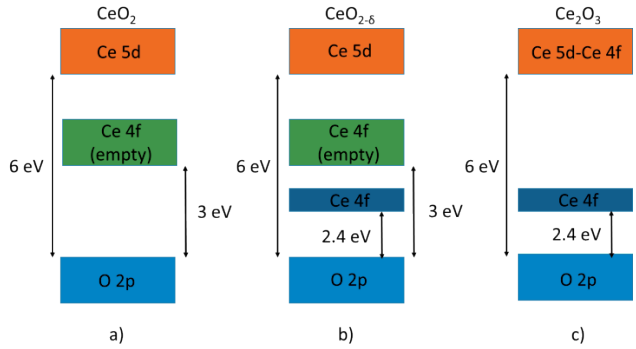

Figure 2. Schematic band diagram for (a) stoichiometric CeO_2, (b) partially reduced CeO_{2-x} and (c) Ce_2O_3.

Figure 2 shows the differences in electronic structure between cerium(IV) oxide, partially reduced cerium(IV) oxide and cerium(III) oxide. The electronic structure of CeO_2 consists of an O 2p based valence band and a Ce 5d based conduction band, between which lies an empty and narrow Ce 4f band (Figure 2a). When an oxygen ion leaves the ceria crystal lattice, a neutral species ½ O_2 is formed, while the two residue electrons become localized at the two nearest cerium sites. The electron at such cerium site is inclined to occupy the empty Ce 4f state, which causes the split of the Ce 4f band into two sub-bands: an empty and a full Ce 4f band (Figure 2b). When all Ce^{4+} ions are reduced to Ce^{3+}, Ce_2O_3 is formed. The electronic band structure of Ce_2O_3 is similar to that of partially reduced ceria, in which the empty Ce4f band and the Ce5d band have fused into the conduction band (Figure 2c). [7, 8, 9]

2.1. Doping

Another way to promote oxygen vacancies formation in cerium(IV) oxide is doping of ceria with elements having lower valence, such as transition metals. Doping is actually the introduction of extrinsic defects into the ceria crystal lattice by incorporation of foreign metal cations (Figure 3).

Studies have shown that doped ceria has better properties than pure ceria, which is attributed to the creation of additional oxygen vacancies and a reduced energy barrier for oxygen migration. Dopants can also modify and stabilize crystallite size and specific surface area of ceria nanoparticles, i.e. increase their resistance to grain growth at elevated temperatures, which is especially important for catalytic applications. [10-12] High oxygen ion conductivities of doped ceria made it of great interest in use as a solid electrolyte in solid oxide fuel cells. [6]

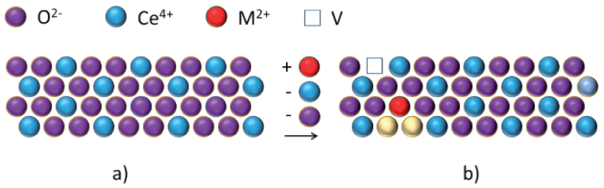

Figure 3. Modification of ceria crystal lattice (a) by incorporation of metal ions having lower valence. As a consequence of replacement of Ce^{4+} ion with M^{2+} ion, oxygen vacancy (V) appears (b).

Figure 2a shows that the band gap value between the O 2p and empty Ce 4f bands is around 3 eV, and that is the band gap value attributed to ceria according to literature. [13, 14] The value indicates that CeO_2 can strongly absorb UV light, but not visible light. Concerning possible photocatalytic and biomedical applications, it would be desirable to reduce the band gap value into the visible light region. Doping with different transition metals can help achieve this due to the aforementioned additional oxygen vacancies formation. When a transition metal ion (M^{2+}) substitutes Ce^{4+}, the number of oxygen vacancies V increases to preserve the charge neutrality (Figure 3). The two residue electrons further promote the reduction of Ce^{4+} to Ce^{3+} and the lattice strain increases. This is then reflected in electronic structure and the result is band gap reduction. In summary, the band gap reduction is due to increased crystal lattice disorder caused by defect states between valance bands and conduction bands. [14]

2.2. Nanocrystalline ceria

Nanotechnology is an ever emerging field which has gained much significance in many industrial branches. This is mainly due to the enhanced properties of nanosized materials in comparison to bulk materials. This phenomenon arises from the fact that nanoparticles of a material have a much larger specific surface area than the same bulk material, which can be better explained by figure 4. Atoms inside the material have all the possible chemical bonds satisfied, while the ones on the surface do not and therefore have higher energy than atoms on the inside, causing them to be more reactive because they tend to reduce their energy. For bulk materials, a far larger proportion of the atoms is situated in the interior, while for nanomaterials the number of surface atoms becomes significant. [16]

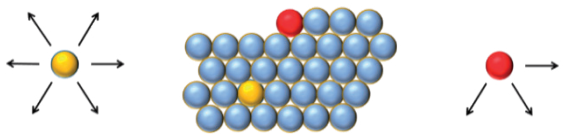

Figure 4. Surface atoms (red) due to unsatisfied chemical bonds have higher energy than atoms inside the crystal lattice (yellow).

Higher energy of surface atoms affects the morphology, reactivity, catalytic potential and other properties of nanomaterials. [16] The energy necessary for defect formation is reduced resulting in an increase in the level of nonstoichiometry and electronic carrier generation in nanocrystalline oxides. [6] Modern research is focused on the preparation, characterization and application of nanosized ceria because of its improved redox properties, transport properties and surface to volume ratio in comparison to bulk ceria. [6, 17]

3. Applications of ceria

The abundance of cerium, high mobility of oxygen vacancies and the reversible valence couple Ce^{4+}/Ce^{3+} make ceria a valuable oxygen storage material with extensive applications in various fields, such as catalysts, low-temperature water-gas shift (WGS) reaction, oxygen sensors, oxygen permeation membrane systems, fuel cells, electrochromic thin-film applications, ion batteries, etc. [7, 18] In the following chapters, few of these applications will be discussed in more detail.

3.1. Solid oxide fuel cells

Solid oxide fuel cells (SOFCs) are power generation systems which depend on electrochemical reactions to produce electricity in contrast to traditional Carnot restricted combustion cycles. High energy conversion efficiency is acquired by a clean, low pollution, reliable and adaptable technology making SOFCs the energy production system of the future. [19, 20]

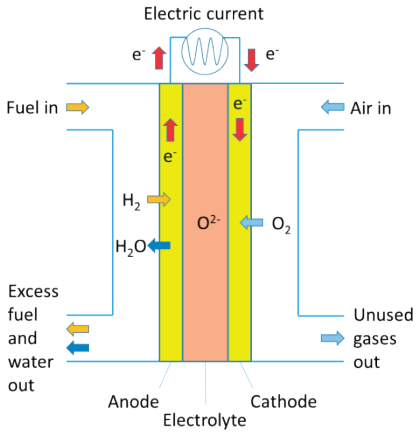

Figure 5. Solid oxide fuel cell components and working principle.

A solid oxide fuel cell consists of two porous electrodes (cathode and anode) between which lies a solid electrolyte (Figure 5). The electrolyte is an oxygen ion conducting material, which means it allows oxygen ions, but not electrons to pass through it. At the cathode, also called the air electrode, oxygen is supplied and it reacts with electrons from the external circuit to form oxygen ions which then migrate through the electrolyte to the anode (fuel electrode). The half reaction at the cathode is as follows:

$$O_2 + 4e^- \rightarrow 2\,O^{2-} \qquad \text{(Eq. 3)}$$

The oxygen ions react with the fuel at the anode. The fuel can be pure hydrogen or a mixture of hydrogen and carbon monoxide, which can be obtained by internal reforming of a hydrocarbon fuel, e.g. methane, with the anode serving as a catalyst for this conversion. [21, 22] The products of the reaction when hydrogen is introduced at the anode are electrons and water vapor. The electrons (electricity) then flow through the external circuit to the cathode in order to keep the overall charge neutrality. The half reaction at the anode is the following:

$$2\,H_2 + 2\,O^{2-} \rightarrow 4\,e^- + 2\,H_2O \qquad \text{(Eq. 4)}$$

Materials for SOFC components need to be carefully selected to enable the whole system to function properly. Some of the criteria are sufficient chemical and structural stability at operating and manufacturing temperatures; minimal reactivity and interdiffusion, as well as matching the thermal expansion between different components. The primary temperature range for SOFCs operation was between 900 and 1000 °C.

The advantages of such high temperatures were the reforming of hydrocarbon fuels and production of high quality heat for cogeneration. However, the reduction of this range to values between 650 and 800 °C opened up the possibility of using a wider range of materials for cell components, simplified the thermal management, enabled a faster start up and cool down, and resulted in less degradation of cell and stack components. The problem at lower temperatures is the decrease of electrolyte conductivity and electrode kinetics, which is why new materials for cell components are being designed and tested. [20, 21]

The most commonly used electrolyte material is yttria stabilized zirconia (YSZ) due to its sufficient ionic conductivity, chemical and thermal stability, and mechanical strength. The disadvantage of YSZ is low ionic conductivity below 750 °C. The use of scandia-doped zirconia, which has higher ionic conductivity, is one possible solution, but high cost of scandium and observed detrimental effects of ageing in scandia-doped zriconia hinder its use in commercial applications. [21, 23, 24] Electrolytes based on doped ceria exhibit a higher ionic conductivity than zirconia based materials (0.025 $(\Omega cm)^{-1}$ for Ce0.9Gd0.1O1.95 in comparison to < 0.005 $(\Omega cm)^{-1}$ for zirconia, at 600 °C), and are also much cheaper due to the abundance of ceria in natural resources. [21, 25] Ceria is usually doped with gadolinium or samarium for its use in solid oxide fuel cells. [19-25] A serious drawback of ceria in this application is its easy reducibility at low oxygen partial pressures, i.e. the reduction of Ce^{4+} to Ce^{3+} and formation of oxygen vacancies, which leads to increasing electronic conductivity and potential mechanical decomposition under large oxygen chemical potential gradients common during SOFC process. [21, 25] This problem can be solved by decreasing the operation temperature below 600 °C, and doped ceria-based materials are being successfully implemented as electrolytes into modern commercial SOFCs, e.g. by Ceres Power Limited (UK). [21, 26]

In addition to being used as an electrolyte, cerium (IV) oxide can also be used in fuel cells as a barrier layer on the cathode to hinder its reaction with the YSZ electrolyte or it can be added to the cathode or anode material to serve as a catalyst. [27] A problem that occurs with hydrocarbon fuels is the accumulation of carbon on the anode which can deactivate and destroy the anode. In order to get around that problem, mixed conductivity and fuel direct oxidation or direct reforming electrocatalytic activity need to be secured. The formation of oxygen vacancies and the existence of electronic conductivity alongside ionic conductivity, which were its drawbacks in the use as electrolyte, are now the benefits of ceria for usage as anode oxidation catalyst. Ceria-based materials are proven to have higher resistance to carbon deposition, meaning that hydrocarbon fuels can be supplied directly to the anode without pre-reforming and purification. [27-30] Doping of ceria enhances the favorable properties, so a lot of research is focused on doped ceria materials, e.g. gadolinium-doped ceria (CGO) [31] and yttria-doped ceria (YDC) [32] The morphology of the catalyst also plays an important role as it can provide extra stabilization and enhance anode efficiency. Examples are work by Adijanto et. al which prepared Pd-CeO_2 core-shell systems that were found to be effective anodic catalysts for hydrogen and methane fuels with extra stability due to the core-shell structure [33] and research by Sun et al. who increased the efficiency of their anode with Ru-CeO_2 by achieving a porous flowerlike microsphere morphology of the CeO_2 support. [34] Research is also done on ceria-alumina systems, which are being extensively used in automotive catalysts where alumina is used as support for ceria catalyst. [27, 28, 35] Since it was noticed that the mechanical stability of ceria is not satisfying under SOFCs operating conditions [36], an idea arose to combine ceria and alumina in order to enhance the mechanical stability, as well as thermal stability of ceria without a negative impact on its ionic conductivity. In that way, $CeAlO_3/CeO_2–Al_2O_3$ nanosized-particle electrocatalyst was prepared which exists as $CeAlO_3$ in a reducing atmosphere and as ceria and alumina in an oxidizing atmosphere. [28]

3.2. Supercapacitors

Supercapacitors, also known as ultracapacitors or electrochemical capacitors, are electrical energy storage devices gaining prominence in recent years. One of the main reasons for the development of supercapacitors is the inevitable depletion of conventional energy sources, meaning that renewable sources will take over energy production industry. Since renewable sources mostly rely on natural phenomena like the sun or wind, which are unpredictable and unstable, renewable energy is not completely reliable. The solution is to find a good way to store the produced energy and then use it later when needed. [37, 38] In addition to batteries, supercapacitors are one of the possible solution methods, with their main advantages over batteries being higher power density, faster charging/discharging rate, good stability and longer cycle-life. [37, 39] A supercapacitor consists of two identical (symmetric supercapacitor) or different (asymmetric capacitor) electrodes with a separator in between them (Fig. 6). The separator is an ion-permeable, but electrically-insulating material placed in an electrolyte which enables ion charge transfer between the electrodes. The material used for the separator depends on the type of the electrolyte used; ceramic or glass-fibers separators are used in aqueous electrolytes, while polymer or paper separators are used in organic electrolytes. [40]

There are a few possible classifications of supercapacitors: type of electrolyte (aqueous or organic), electrode material (carbon-based materials, transition metal oxides, and conductive polymers) and charge storage mechanism (electrochemical double layer capacitors - EDLCs, faradic pseudocapacitors, and hybrid capacitors. [41] Ceria/graphene composites are mainly studied as electrodes in pseudocapacitors. Pseudocapacitors store energy through rapid and reversible electrochemical redox reactions which occur on the interface between the electrodes and the electrolyte, making high specific surface area and high electrical conductivity crucial factors for electrode materials in high-performance pseudocapacitors.

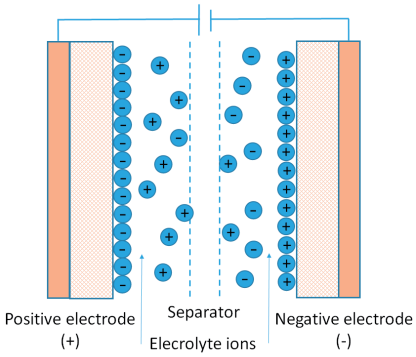

Figure 6. Schematic representation of electrical double-layer capacitor.

Graphene or other carbon based materials are in this case used as substrates for deposition of active materials and/or as current collectors which secure high capacitance and fast charge transfer of the electrodes. The active component is usually a metal oxide or a conductive polymer. As metal oxides are concerned, the metals used must have at least two oxidation states, which can coexist and be freely and easily interchanged. [40] Ceria has two stable oxidation states and an easy transition between the states is possible without the collapse of crystal structure. Per se, ceria can store charge electrochemically by Faradaic redox reactions or by non-Faradaic process through electric-double layers. For better understanding, equations 5 and 6 present the non-Faradaic and Faradaic process for a ceria electrode when KOH is used as electrolyte [42]:

Faradaic process:

$$CeO_2 + K^+ + e \rightarrow Ce^{3+}\,OOK \qquad \text{(Eq.5)}$$

Non-Faradaic process:

$$(CeO_2)_{surface} + K^+ + e \rightarrow (CeO_2\,K^+)_{surface} \qquad \text{(Eq.6)}$$

Both processes occur on the surface of the electrode and are therefore highly dependent on its specific surface area. The use of nanosized ceria instead of bulk one enhances the charge-storage performance due to the higher specific surface area of nanomaterials. Additional improvements can be achieved by doping. Ghosh et al. studied Zr doped ceria and reported on the enhancement of pseudocapacitive behavior of ceria due to incorporation of Zr ions into the ceria crystal lattice. Namely, doping promotes the formation of oxygen vacancies and the redox reaction between Ce^{4+} and Ce^{3+} ions, which induces higher Faradaic contribution to charge-storage. Furthermore, doping causes the reduction of average crystallite size and average particle size which in turn increases the specific surface area and improves the non-Faradaic contribution. [42]

3.3. Catalytic application

Ceria is extensively used as a heterogeneous catalyst in many technologically important processes. Traditional catalysts, namely noble metals are expensive, scarce in resources, sensitive to high temperatures and susceptible to poisoning. Cerium (IV) oxide is being imposed as a viable alternative because it has suitable properties like low cost, availability, low sensitivity to high temperatures and good resistance to poisoning, while at the same time enabling high conversions for certain types of chemical processes. Cerium (IV) oxide is used as a catalyst and promotor in three-way catalytic converters in car exhaust systems [35], for the conversion of water-gas, also known as synthesis gas - a mixture of carbon monoxide and hydrogen, to produce hydrogen for various industrial processes [43, 44], in self-cleaning ovens [45], and for the removal of atmospheric pollutants such as volatile organic compounds [14, 46].

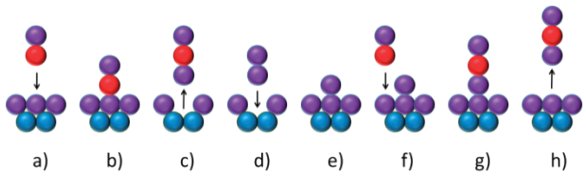

Figure 7. Carbon monoxide oxidation process in presence of ceria catalyst. Blue dots represent cerium atoms, magenta dots oxygen atoms and red dots carbon atoms.

The catalytic activity of ceria can be illustrated on carbon monoxide oxidation process (Figure 7). CO molecule is adsorbed onto the ceria surface (a). The ease of formation of oxygen vacancies facilitates the reaction between CO and surface oxygen (b). The formed carbon dioxide diffuses away leaving an oxygen vacancy (c), where a new oxygen molecule is then adsorbed (d). The presence of oxygen vacancy enables the reaction of the adsorbed oxygen molecule with the ceria surface, thereby weakening the bond between oxygen atoms in the molecule (e). Another CO molecule adsorbs on the surface (f), diffuses to the excess oxygen and reacts with it (g) and diffuses away from the surface (h). This particular reaction occurs in the exhaust system of automobiles and ceria is commercially applied as a catalyst in this process. [47, 48] Hence, a more detailed explanation of automotive catalytic converters is due.

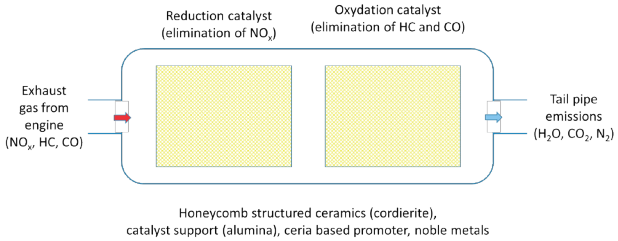

Figure 8. Basic components of a three-way catalytic converter.

Figure 8 shows the basic components of a three-way catalytic (TWC) converter in automotive exhaust systems. The term three-way pertains to the three types of pollutants it helps to reduce: nitrogen oxides (NO_x), carbon monoxide (CO) and hydrocarbons (HC). Basically, three reactions happen simultaneously inside the TWC converter: [35]

1. Reduction of nitrogen oxides into elemental nitrogen and oxygen
2. Oxidation of carbon monoxide to carbon dioxide
3. Oxidation of hydrocarbons into carbon dioxide and water

Therefore, three-way catalytic converters utilize two types of catalyst – a reduction and an oxidation catalyst. Both of them typically consist of a monolithic support which is usually made of cordierite and has a honeycomb structure insuring the best possible contact between the catalyst and exhaust gases. The honeycomb consists of channels whose inner surface is coated with the catalytically active material. This material is composed of a thermally stable support (most common being Al_2O_3), the active phase which are mainly noble metals (Pt and/or Pd for oxidation reactions and Rh for reduction reactions) and a ceria-based promoter (typically $Ce_xZr_1{-}xO_2$). The gas phase coming from the engine into the converter constantly and rapidly oscillates between lean (air-to-fuel ratio > 14.6) and rich conditions (air-to-fuel ratio < 14.6). In order to operate properly, a three-way catalytic converter must first reduce the NO_x compounds during rich conditions and then oxidize CO and HC during lean conditions. The main role of ceria is to act as oxygen buffer: reduced ceria ($CeO_2{-}\delta$) is capable of storing oxygen during lean-to-rich transition and thereby promoting the reduction of NOx, while it is at the same time able to provide the oxygen necessary for CO and HC oxidation during rich-to-lean transition. [27, 35] The application of ceria in three-way catalytic converters is one of the well-established applications, but is far from being the sole one and many of the ceria applications mentioned in this work will soon find their way to larger commercial utilization.

4. Hydrothermally derived cerium(IV) oxide

Our group has been dealing with ceria for several years, focusing on the preparation of different ceria nanostruc-

tures, trying out different synthesis methods and different dopants for the enhancement of ceria properties. The most detailed research was conducted in the preparation of ceria nanoparticles prepared by hydrothermal synthesis and aimed for catalytic application, in the oxidation of volatile organic compounds. [14, 46, 49, 50]

Preliminary research included the doping of ceria with the same amount of various transition metals to enable the comparison of catalytic activity and overall influence of the dopant on the properties of ceria. [14] Doping with copper, manganese and zinc proved to be the most beneficial for the overall properties of ceria, resulting in spherical nanoparticles of very small sizes (~ 4 nm) and high specific surface areas (~ 200 $m^2 g^{-1}$), as well as very good catalytic activity as shown in Figure 9. Therefore, these metals were chosen for further research, and special emphasis was placed on copper and manganese. Ceria was doped with 10, 20, 30 and 40 mol. % of Cu, and 10, 20 and 30 mol. % of Mn.

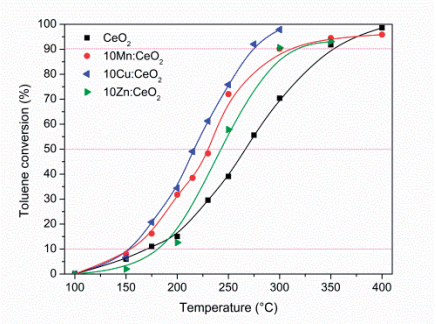

Figure 9. Preliminary catalytic activity results for pure and transition metal doped samples.

The as-prepared samples doped with manganese showed crystallite sizes around 4 nm, while those of samples doped with copper were around 3.3 nm, which is unprecedented for this synthesis method. Besides ceria, the manganese doped samples showed the presence of monoclinic sodium birnessite, $Na_{0.55}Mn_2O_4 \cdot 1.5\ H_2O$, which consists of octahedral MnO6 sheets with Na ions and crystal H_2O molecules in the interlayer. [51] The said birnessite transforms into romanechite-like sodium manganese oxide, $Na_2Mn_5O_{10}$, upon thermal treatment at 500 °C. However, the presence of an additional phase does not have a negative effect on the properties of CeO_2. The specific surface area and thermal stability of the samples increases with the increase of the manganese amount. [50] The beneficial influence of manganese on the overall properties of ceria culminates in its catalytic activity. The catalytic activity of Mn doped samples in the process of toluene oxidation is significantly higher than that of pure ceria sample.

The copper doped samples exhibit no additional phases except ceria, which indicates that copper is incorporated into the CeO_2 crystal lattice forming a solid solution. All copper doped samples have better overall properties than pure ceria, in terms of thermal stability, higher amount of oxygen vacancies and lower band gap values, proving the doping advantageous. However, there is no drastic difference between the doped samples, with the exception being the 40 mol. % Cu doped ceria sample. This sample possesses the highest thermal stability, the highest number of oxygen vacancies as determined by XPS analysis, a distinct bimodal pore size distribution after thermal treatment at 500 °C which facilitates molecular transport and reduces diffusion limitations present in narrow uniform pores, and the lowest band gap value (2.71 eV) which is extremely favorable for photocatalytic applications. [52] These results are also reflected in the best catalytic activity of 40 mol. % Cu doped sample in the BTEX (benzene, toluene, ethylbenzene and o-xylene) oxidation process. [49]

The hydrothermal method proved to be a simple, yet efficient method for the preparation of pure and doped ceria samples of high purity, small crystallite sizes, excellent properties and very good catalytic activity in the oxidation of volatile organic compounds.

5. Conclusion

Cerium (IV) oxide is a material capable of a facile reversible redox process which enables the creation of oxygen vacancies, high oxygen mobility and oxygen storage capacity within the crystal lattice. This key feature of ceria allows its use in many different fields, while the introduction of nanostructural design and doping with metal ions of lower valence further enhance the overall advantageous properties of ceria and open up the possibility of creating new materials with improved properties.

6. Acknowledgements

This work has been fully supported by the Croatian Science Foundation under the project IP-01–2018-2963. The sustenance of the University of Zagreb is gratefully acknowledged. The fruitful discussion with M. Metikoš-Huković and S. Omanović is much obliged.

7. References

1. Borra, C.R., Vlugt, T.J.H., Yang, Y., Offerman, S.E. Recovery of Cerium from Glass Polishing Waste: A Critical Review, Metals 8 (2018) 801.
2. Voncken, J.H.L. The Rare Earth Elements, Chapter 3: Physical and Chemical Properties of the Rare Earths, Springer International Publishing, 2016, pp. 53-72.
3. Dunnick, K.M., Morris, A.M., Badding, M.A., Barger, M., Stefaniak, A.B., Sabolsky, E.M., Leonard, S.S. Evaluation of the effect of valence state on cerium oxide nanoparticle toxicity following intratracheal instillation in rats, Nanotoxicology 10 (7) (2016) 992–1000.
4. Arenas, L.F., Ponce de León, C., Walsh, F.C. Electrochemical redox processes involving soluble cerium species, Electrochim. Acta. 205 (2016) 226-247.
5. Mogensen, M., Sammes, N.M., Tompsett, G.A. Physical, chemical and electrochemical properties of pure and doped ceria, Solid State Ion. 129 (2000) 63-94.

6. Sun, C., Li, H., Chen, L. Nanostructured ceria-based materials: synthesis, properties, and applications, Energy Environ. Sci. 5 (2012) 8475-8505.
7. Younis, A., Chu, D., Li, S. Chapter 3: Cerium Oxide Nanostructures and their Applications, in Functionalized Nanomaterials, Editor: M. A. Farrukh, IntechOpen, 2016, http://dx.doi.org/10.5772/65937.
8. Castleton, C.W.M., Lee, A.L. Description of polarons in ceria using Density Functional Theory, J. Phys.: Conf. Ser. 526 (2014) 012002, https://doi.org/10.1088/1742-6596/526/1/012002.
9. Shoko, E., Smith, M.F., McKenzie, R.H. A consistent picture of the charge distribution in reduced ceria phases, 2009, arXiv:0910.0669 [cond-mat.str-el].
10. Tan, J., Zhang, W., Lv, Y.H., Xia, A.L. Facile Preparation of Mn-doped CeO2 submicrorods by composite-hydroxide-salt-mediated approach and their magnetic property, Mat. Res. 16 (2013) 689-694.
11. Kurajica, S., Munda, I.K., Brleković, F., Mužina, K., Dražić, G., Šipušić, J., Mihaljević, M. Manganese-doped ceria nanoparticles grain growth kinetics, Journal of Solid State Chemistry, 291 (2020) 121600.
12. Liu, L., Shi, J., Zhang, X., Liu, J. Flower-Like Mn-doped CeO2 microstructures: synthesis, characterizations, and catalytic properties, J. Chem. 254750 (2015) 1–11.
13. Zhang, T., Kumar, E., Selvarajana, P., Muthuraj, D. Synthesis and characterization of CeO2 nanocrystals by solvothermal route, Mater. Res. 16 (2013) 269–276.
14. Kurajica, S., Mužina, K., Dražić, G., Matijašić, G., Duplančić, M., Mandić, V., Župančić, M., Munda, I.K. A comparative study of hydrothermally derived Mn, Fe, Co, Ni, Cu and Zn doped ceria nanocatalysts, Mater. Chem. Phys. 244 (2020) 122689, https://doi.org/10.1016/j.matchemphys.2020.122689.
15. Tiwari, S., Rathore, G., Patra, N., Yadav, A.K., Bhattacharaya, D., Jah, S.N., Tseng, C.M., Liu, S.W., Biring, S., Sen, S. Oxygen and cerium defects mediated changes in structural, optical and photoluminescence properties of Ni substituted CeO2, J. Alloy. Comp. 782 (2019) 689–698.
16. Kurajica, S., Lučić Blagojević, S. Uvod u nanotehnologiju, HDKI, Zagreb, 2017.
17. Lopez, J.M., Gilbank, A.L., Garcıa, T., Solsona, B., Agouram, S., Torrente-Murciano, L. The prevalence of surface oxygen vacancies over the mobility of bulk oxygen in nanostructured ceria for the total toluene oxidation, Appl. Catal., B, 174-175 (2015) 403–412.
18. Tang, W.X., Gao, P.X. Nanostructured cerium oxide: preparation, characterization, and application in energy and environmental catalysis, MRS Communications 6 (2016) 311–329.
19. Sumi, H,. Shimada, H., Yamaguchi, Y., Yamaguchi, T. Metal-supported microtubular solid oxide fuel cells with ceria-based electrolytes, J. Ceram. Soc. Jpn. 125 (4) (2017) 208-212.
20. Brown, E.C. Electrochemically Deposited Ceria Structures for Advanced Solid Oxide Fuel Cells, Doctoral thesis, California Institute of Technology, Pasadena, California, 2011.
21. Singhal, S.C. Solid Oxide Fuel Cells, The Electrochemical Society Interface 16 (4) Winter (2007) 41-44.
22. Singhal, S.C., Kendall, K. High temperature solid oxide fuel cells: fundamentals, design and applications, Elsevier, Oxford, 2003.
23. Pikalova,E.Yu., Bamburov, V.G., Murashkina, A.A., Neuimin, A.D., Demin, A.K., Plaksin, S.V. Solid Electrolytes Based on CeO2 for Medium Temperature Electrochemical Devices, Elektrokhimiya 47 (6) (2011) 738–744.
24. Pikalova, E.Yu., Kolchugin, A.A., Bamburov, V.G. Ceria-based materials for high-temperature electrochemistry applications, Int. J. of Energy Prod. & Mgmt. 1 (3) (2016) 272–283.
25. Kharton, V. V., Figueiredo, F.M., Navarro, L., Naumovich, E.N., Kovalesky, A.V., Yaremchenko, A.A., Viskup, A.P., Carneiro, A., Marques, F.M., Frade, J.R. Ceria-based materials for solid oxide fuel cells, J. Mater. Sci. 36 (2001) 1105-1117.
26. https://www.cerespower.com/ (Access: 28.1.2020.)
27. Montini, T., Melchionna, M., Monai, M., Fornasiero, P. Fundamentals and Catalytic Applications of CeO_2-Based Materials, Chem. Rev. 116 (2016) 5987−6041.
28. Venancio, S.A., de Miranda, P.E.V. Synthesis of $CeAlO_3$/CeO_2–Al_2O_3 for use as a solid oxide fuel cell functional anode material, Ceram. Int. 37 (2011) 3139–3152.
29. Park, S., Vohs, J., Gorte, R. Direct Oxidation of Hydrocarbons in a Solid-Oxide Fuel Cell, Nature 404 (2000) 265−267.
30. Gorte, R.J., Vohs, J.M. Nanostructured Anodes for Solid Oxide Fuel Cells, Curr. Opin. Colloid Interface Sci. 14 (2009) 236−244.
31. Marina, O.A., Bagger, C., Primdahl, S., Mogensen, M. A Solid Oxide Fuel Cell with a Gadolinia-Doped Ceria Anode: Preparation and Performance, Solid State Ion. 123 (1999) 199−208.
32. Murray, E.P., Tsai, T., Barnett, S.A. A Direct-Methane Fuel Cell with a Ceria-Based Anode, Nature 400 (1999) 649−651.
33. Adijanto, L., Sampath, A., Yu, A.S., Cargnello, M., Fornasiero, P., Gorte, R.J., Vohs, J.M. Synthesis and Stability of Pd-CeO2 Core−Shell Catalyst Films in Solid Oxide Fuel Cell Anodes, ACS Catal. 3 (2013) 1801−1809.
34. Sun, C., Xie, Z., Xia, C., Li, H., Chen, L. Investigations of Mesoporous CeO2−Ru as a Reforming Catalyst Layer for Solid Oxide Fuel Cells, Electrochem. Commun. 8 (2006) 833−838.
35. Ramakrishnan, G., Naveen, K. Emission and dynamic characteristics of three way catalytic converter by computational fluid dynamics, Int. J. Eng. Sci. 6 (2016) 3503-3510.
36. Prakash, A.S., Shivakumara, S., Hegde, M.S. Single step preparation of CeO2/CeAlO3/g-Al2O3 by solution combustion method: Phase evolution, thermal stability and surface modification, Mater. Sci. Eng. B 139 (2007) 55–61.
37. Saravanan, T., Shanmugam, M., Anandan, P., Azhagurajan, M., Pazhanivel, K., Arivanandhan, M., Hayakawad, Y., Jayavel, R. Facile synthesis of graphene-CeO2 nanocomposites with enhanced electrochemical properties for supercapacitors, Dalton Trans. 44 (2015) 9901–9908.
38. Dezfuli, A.S., Ganjali, M.R., Naderi, H.R., Norouzi, P. A high performance supercapacitor based on a ceria/graphene nanocomposite synthesized by a facile sonochemical method, RSC Adv.5 (2015) 46050-46058.

39. Lokhande, C.D., Dubal, D.P., Joo, O.S. Metal oxide thin film based supercapacitors, Curr. Appl. Phys. 11 (2011) 255-270.
40. Chen, X., Paul, R., Dai, L. Carbon-based supercapacitors for efficient energy storage, Natl. Sci. Rev. 4 (3) (2017) 453–489.
41. Shishesaz, M., Sarpoushi, M.R., Golozar, M.A. An Electrochemical Investigation of Nano Cerium Oxide/ Graphene as an Electrode Material for Supercapacitors, Iranian Journal of Oil & Gas Science and Technology 4 (1) (2015) 81-91.
42. Ghosh, S., Thomas, T., Rao, G.R. Zr substitution aided enhancement of pseudocapacitive behavior of ceria, Mater. Lett. (2020), doi: https://doi.org/10.1016/j.matlet.2020.127500.
43. Ren, Z., Peng, F., Li, J., Liang, X., Chen, B. Morphology-dependent properties of Cu/CeO2 catalysts for the water-gas shift reaction, Catalysts 7 (2017) 48.
44. Si, R., Raitano, J., Yi, N., Zhang, L., Chan, S., Flytzani-Stephanopoulos, M. Structure sensitivity of the low-temperature water-gas shift reaction on Cu–CeO2 catalysts, Catal. Today 180 (2012) 68-80.
45. Palmisano, P., Russo, N., Fino, D., Saracco, G., Specchia, V., Faraldi, P., Polverini, D., Arteconi, L. Doped ceria catalysts for an innovative self-cleaning domestic oven, 21st North American Catalysis Society Meeting 2009, Proceedings 1 (2009) 341-342.
46. Duplančić, M., Kurajica, S., Tomašić, S., Minga, I. Catalytic oxidation of toluene on hydrothermally prepared ceria nanocrystals, Chem. Biochem. Eng. Q. 31 (2017) 375-383.
47. Conesa, J.C., Martinez-Arias, A., Fernandez-Garcia, M., Soria, J. Surface Structure and Redox Chemistry of Ceria-Containing Automotive Catalytic Systems Res. Chem. Intermed., 26 (2000) 103-111.
48. Campbell, C.T., Peden, C.H.F. Chemistry - Oxygen Vacancies and Catalysis on Ceria Surfaces. Science, 309 (2005) 713-714.
49. Mužina, K., Kurajica, S., Guggenberger, P., Duplančić, M., Dražić, G. Catalytic activity and properties of copper-doped ceria nanocatalyst for VOCs oxidation, *J. Mater. Res.* 37 (2022) 1929-1940.
50. Kurajica, S., Ivković, I.K., Dražić, G., Shvalya, V., Duplančić, M., Matijašić, G., Cvelbar, U., Mužina, K. Phase composition, morphology, properties and improved catalytic activity of hydrothermally-derived manganese-doped ceria nanoparticles, *Nanotechnology* 33 (13) (2022) 135709.
51. Kurajica, S., Munda, I.K., Dražić, G., Mandić, V., Mužina, K. Bauer, L., Matijašić, G. Manganese-doped, hydrothermally-derived ceria: The occurrence of birnessite and the distribution of manganese, *Ceram. Int.* 46 (18) (2020) 29451-29458.
52. Mužina, K., Kurajica, S., Dražić, G., Guggenberger, P., Matijašić, G. True doping levels in hydrothermally derived copper-doped ceria, *J. Nanopart. Res.* 23 (2021) 149. 57

Floren Radovanović-Perić[1], Ivana Panžić[1], Arijeta Bafti[1], Marko Rukavina[1], Andrea Jurov[1], Vilko Mandić[1]

Showcase of tools for preparing, modifying and describing thin films for energy conversion devices with special attention on plasma phenomenology

[1]Faculty of Chemical Engineering and Technology, University of Zagreb, Trg Marka Marulića 20, 10000 Zagreb, Croatia

Abstract

This paper draws attention to the wide range of capacities of the Group, including chemical and physical deposition, modification and processing techniques, and advanced characterisations. In particular, this work demystifies the new plasma discharge method for the synthesis of thin films, which is still under development. Specifically, the coupled spark plasma ablation deposition (SPAD) can be performed at almost ambient conditions in various configurations with respect to several deposition reactors, proving powerful, versatile, green, and easy-to-use nature of the method. Composition-wise, up to 4 element material can be derived combining pure electrodes, however the derived composition can be broader when using alloy electrodes. It is indisputable that SPAD is capable of producing thin films at a significantly reduced cost compared to other methods.which we want to put in use for the constituent layers of the last generation of energy conversion devices. Generally, the SPAD optimisation envelope heavily differs for the case of intended products: nanoparticle vs thin film, or metal vs metal oxide, or crystalline vs amorphous. Here, we will provide a more detailed description of the ablation parameters that are necessary to achieve the various crystallinities of nanomaterials. Copper nanoparticles and thin films were derived via SPAD and additionally thermally treated. (Micro)structural and thermal evolution points out to interesting development of the surface morphologies. In addition, the results enabled the correlation between oxygen plasma concentration and order of crystallinity in the thin films.

***Keywords**: spark ablation; plasma; nanomaterial; thin film; copper oxide.*

1. Introduction

Metallic and metal oxide nanoparticles attract considerable attention in various applications, such as biomedicine [1–3], optoelectronics [4], [5], energy conversion [6–9] and catalysis [10–12]. The quantum confinement effect and surface-to-volume ratio are the most interesting properties of metallic nanoparticles. Surface area, which increases with decreasing nanoparticle size, influences the interaction between nanoparticles and other reactive substances and consequently can enhance their performance in various applications. For some applications, such as energy conversion devices, it is useful to have nanoparticles in a thin film configuration. The necessary routes are covered within chemical and physical depositions, where the Group developed board expertise. Chemical depositions are more flexible and generally more economical, however they do not have the capability to modify the spatial delineation of the domains. A chemical deposition technique usually starts with some sort of solution chemistry process that has to be controlled to a desired time domain; from a long time domain for e.g. ambient humidity controlled yield of nanoparticles, to levels of short time domains for e.g. dip coating, to spin coating, to spray coating deposition of thin films. Generally, physical deposition techniques are often more specific, less economic, but quite precise. The Group developed expertise for all major thin film production techniques, including: magnetron sputtering (MS), thermal or e-beam evaporation (EBE), and pulsed laser deposition (PLD).

The ablation group of deposition technologies encompasses a wide range of chemical and physical processes, and are widely used in the synthesis of nanomaterials. There are two main ablation technologies available: laser ablation and spark-based ablation. These techniques are both green and efficient methods for nanomaterial synthesis. Spark plasma ablation deposition (SPAD) is based on the sudden sublimation of material from electrodes by inducing spark discharges between them, from which nanoparticles form by condensation [13]. Laser ablation is a highly studied and used technique, but it has certain disadvantages, such as the high cost and complexity of the setup [14]. To simplify the experimental setup, spark ablation is nowadays more often utilised. This type of ablation does not need a laser or vacuum, which reduces the cost of the procedure, is environmentally friendly as it needs no chemical precursors nor produces waste, and is highly scalable [15–16]. A spark discharge generator has a relatively simple design where the key components are two metal electrodes positioned with a small gap between them. Spark ablation is a technique where a metallic target, bombarded with high energy, loses localised atoms in the form of vapour and gives enough energy to the inert gas in its surroundings to form plasma. The inert gas in the state of plasma provides a clean environment for the formation of nanoparticles, and due to its rapid quenching effect, smaller nanoparticles can be formed [17]. In addition, in comparison with chemical methods for nanoparticle synthesis, spark ablation provides a clean synthesis with extremely high efficiencies and purity of the product, which depends only on the purity of the precursor.

The duration of the spark events that induce ablation may affect the size of the resulting particles. Smaller particles can be created by using shorter sparks. Also, shorter sparks help avoid continuous arcing, which would lead to effects like distillation that disable the possibility of producing mixed particles with controlled composition [15]. The size of the nanoparticles generated is typically less than 20 nm.

Another possibility with spark ablation is to easily produce mixed nanomaterials by using alloy electrodes. With different electrode configurations, it is possible to get an alloy of more than two materials. Additionally, this technique can produce ordered agglomerates and nanostructures consisting of more primary particle species. This is an ablation process specialty, as other nano-material synthesis techniques do not work at this scale to create mixtures. Another possibility is to coat or decorate produced particles [15].

Spark generation is a fast and short process that occurs when the breakdown voltage between the electrodes is reached. The breakdown voltage is quite high and depends on the gas pressure and inter-electrode gap. When the breakdown voltage is surpassed, the ionisation of the gas occurs along with increasing current, accompanied by an intense light emission – plasma. The formation of plasma is dependent on the electrical circuit and the gas in the environment and is capable of producing a variety of discharge types, including glows, arcs, sparks and corona [18]. The temporal evolution of sparks can be characterised by four stages – pre-breakdown, breakdown, arc and afterglow. All four stages have different physical characteristics and, consequently, different contributions to the ablation process [15]. Pre-breakdown and breakdown are dominated by gas emission; in pre-breakdown molecular bands are observed, whereas, in the breakdown, the main emitters are ions, followed by continuous radiation. The breakdown should complete rapidly, in less than 100 ns. The manifestation of a completed breakdown is the arc, which occurs when a conducting channel connects the electrodes. The arc stage is characterised by a large electrical current that heats the electrodes locally which leads to the ablation of the electrode material. This stage is optically defined by light emission of both the species from the ambient gas and electrode material. The arc usually occurs in less than a microsecond after the breakdown. Lastly, there is an afterglow stage where the light emission does not cease even after the current terminates. This emission comes from the metastable species of the ambient gas lingering in and around the spark gap, characterised by lower gas temperature and lower pressure. The afterglow stage can last between tens of microseconds and a couple of milliseconds if another spark has not occurred. The most important stages for nanoparticle production are the arc and the afterglow because most material is ablated during arcing, and the formation of nanoparticles takes place in the afterglow.

However, while spark ablation holds great potential in all fields of nanoparticle research, there is still much work to be done in order to fully understand the effects of process parameters on each oxidation state, phase, particle size distribution, morphology and nanoporosity of the deposited materials.

Thanks to their chemical stability and non-toxicity, copper oxide (Cu_xO_y) nanostructured thin films have recently found many useful applications as low-cost materials in energy conversion fields. Stable Cu_xO_y phases include Cu_2O (cuprite) and CuO (tenorite), while there are numerous metastable phases, amongst them Cu_4O_3 (paramelaconite), an oxide of copper intermediate between the two, corresponding to the formula $Cu_2O{\cdot}(CuO)_2$. CuO and Cu_2O films are generally believed to be p-type semiconductors with band gap energies in visible and near-infrared regions [19]. Moreover, they have high absorption coefficients making them highly promising candidates for active layers in solar cells [20], optoelectronic detectors [21] or sensors [22].

Nanostructured copper oxide thin films can be prepared by several methods: sol-gel, magnetron sputtering, thermal oxidation, hydrothermal, spray pyrolysis, microwave-assisted etc. While all these methods can produce different morphologies and nanostructures, their main disadvantage is expensive equipment to achieve ultra-high vacuum or controlled heating and cooling steps, expensive reagents or low reproducibility. Thin metallic oxide films produced by reactive spark ablation ensure high purity of the material and can be prepared easily in the nanometre range by introducing oxygen into the gas flow. The oxygen reacts with the nanoparticles immediately after their creation. Theoretically, complete conversion is possible at room temperature, in contrast to the commonly used chemical syntheses, which require thermal treatment after deposition.

From the aforementioned, it is obvious that SPAD is one of the few methods that are capable of producing stable metallic oxide nanosized thin films at both ambient temperature and pressure in a time range spanning from no more than a few seconds to a few minutes. In this segmental study, we will focus on the characterisation of the as-prepared thin films at room temperature derived by spark ablation and after their thermal evolution to CuO.

2. Materials and methods

The following materials and chemicals were used: Copper electrodes (6 mm thickness, 99.9% purity, VSParticle, Delft, Netherlands), isopropanol (p.a. Lachner, Zagreb, Croatia).

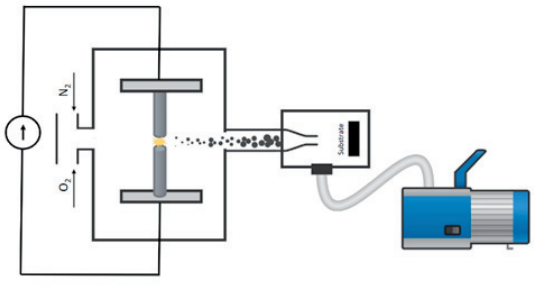

Figure 1. Schematic representation of the SPAD system setup for copper oxide synthesis and subsequent thin film formation.

For the purpose of this research, spark plasma ablation deposition (SPAD) was configured in a crossflow vacuum-assisted impaction deposition setup depicted by the scheme below (**Figure 1**, model, VSParticle, Delft, Netherlands). Two gases, a carrier gas (nitrogen) and a reactive gas (oxygen), are introduced into the reactor containing two copper electrodes. After reaching the breakdown voltage, nanoparticle formation and copper oxidation occur, and the particles are carried away from the electrodes to the deposition chamber. Before reaching the nozzle, the aerosol flow is concentrated and accelerated by narrowing the tube diameter. Upon reaching the vacuum chamber, the aerosol gains a significant kinetic energy boost due to the difference in pressures between the reaction and deposition chamber. The width of the aerosol jet upon impaction is controlled by nozzle width, chamber vacuum pressure (2-200 mbar) and substrate to nozzle distance. Spark discharge was performed in two extremely different atmospheres; 0.07 slpm and 1.05 slpm of oxygen in a total flow of 10 slpm. Thin films were deposited on Si wafers that were previously immersed in isopropanol in an ultrasonic bath for 15 minutes and then exposed to ozone for 15 minutes to remove all of the organic waste at the surface.

Grazing incidence X-ray diffraction was used to study and characterize the thin film crystal structure and its thermal evolution. Patterns were collected using synchrotron radiation (MCX beamline of the Elettra Synchrotron Trieste) using 4-axis Huber goniometer, at 10 keV, step 0.02° 2theta, retention time 0.7 sec in a 2θ range of 5–70° with at grazing angle of 0.5 theta.

Particle and thin film morphologies were observed by two scanning electron microscopes (SEM, Prisma E, Thermo Fisher Scientific Inc., Massachusetts, USA; and JSM 700F, Jeol Ltd., Akishima, Tokio, Japan).

Gas-phase analysis of plasma was conducted by optical emission spectroscopy with a broad-range spectrometer (model LR1, ASEQ Instruments, Vancouver, Canada).

3. Results and discussion

3.1. Plasma analysis

The gas phase plasma diagnostic was conducted with optical emission spectroscopy – a simple tool that has the ability to identify excited species inside the plasma. This method allows one to pinpoint atomic transitions that possibly participate in nanoparticle formation. **Figure 2** presents emission spectra taken during copper ablation with two gas mixtures of nitrogen and oxygen. Nitrogen gas flow was fixed at 10 slpm, but oxygen gas flow was varied between a lower flow of 0.07 slpm and a higher flow of 1.05 slpm.

Both spectra show the same excited atomic species of copper (Cu i from 325 to 329 nm, and Cu ii from 248 to 302 nm), nitrogen (N i, N ii, and N iii from 325 to 940 nm) and oxygen (O i from 715 to 927 nm). The lack of molecular bands in the OES indicates high plasma temperature, as it takes a lot of energy to break molecular bonds and ionize atoms. The main difference between spectra taken for different oxygen flow concentrations is in the emission intensity of all present excited species. For higher oxygen gas flow of 1.05 slpm, emission intensities are also higher, implying that the oxygen concentration in the gas mixture is directly responsible for the excitation of all present plasma species.

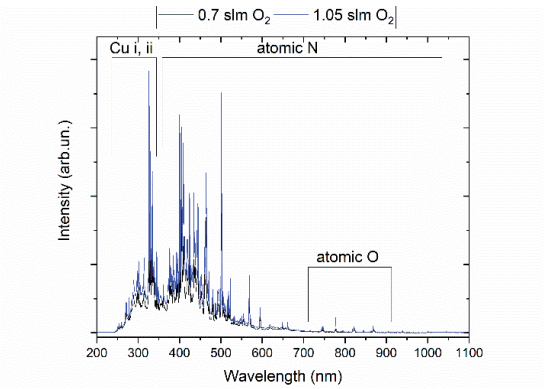

Figure 2. Optical emission spectra of plasma during nanoparticle synthesis for gas mixtures of N_2 and O_2 with line analysis

3.2. Structural ordering and potential for lattice oxygen defect engineering

Diffractograms in **Figure 3** show a crystalline film even at room temperature, where copper and cuprite phases are present. With increasing temperature, the film oxidizes, with a cuprite/tenorite mixed phase system being present at 160 °C, where cuprite is the dominant phase, which can be concluded from the intensity of the Cu_2O diffraction maxima. The cuprite phase further oxidizes, leading to a tenorite dominant phase at 350 °C. However, even at 350 °C, where complete oxidation to tenorite for nanosized copper is expected, the oxidation is incomplete, indicating a fair amount of aggregation [23].

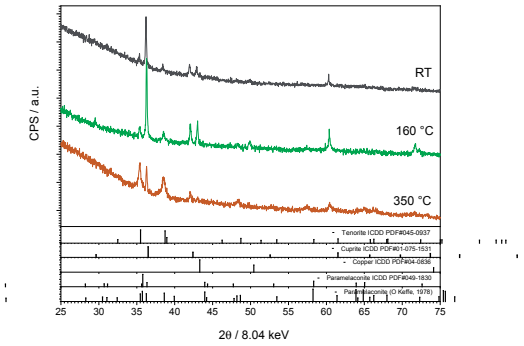

Figure 3. GIXRD patterns of thin films synthesized at 0.07 slpm O_2 thermally treated to various temperatures.

Figure 4 shows patterns of completely amorphous thin films at room temperature. The thermal treatment triggers oxidation, following the same evolutionary pathway as for the sample deposited with a lower amount of oxygen. A mixed tenorite/cuprite phase appears at an intermediate temperature, finally reaching a dominant tenorite system at 350 °C. In both samples, various unidentified diffraction peaks appear, which can all be contributed to mainly paramelaconite phases and a variety of copper oxides with more complex stoichiometries (Cu_xO_y). This is a characteristic of reactive plasma processes where condensation, oxidation and particle formation occur very fast without a solvent, which results in a somewhat uncontrollable process. Generally, during very high local temperatures reached during sparking (~15 000 K), one can expect the formation of only the most thermodynamically favoured phases. However, we show that metastable phases, such as cuprite, paramelaconite and other complex oxides, can be trapped with finely tuned spark and physical deposition parameters. These can all be described as one unique and useful feature spark plasma can provide in nanomaterial synthesis – oxygen lattice defects. These defects are related to the nature of oxygen plasma (a variety of oxygen ion species) inside the reactor and its concentration. It can be said that with increasing the amount of oxygen, more vacancies and defects are introduced into the lattice, resulting in a highly disordered structure, as can be seen for as-synthesized thin films at higher flow rates of oxygen.

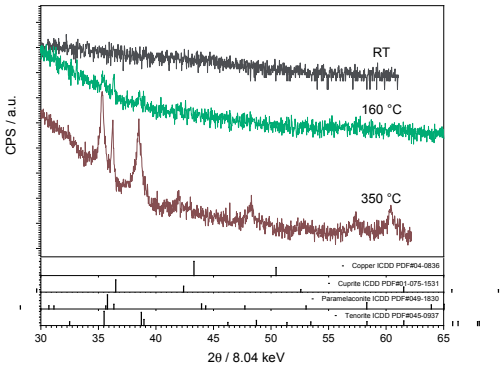

Figure 4. GIXRD patterns of thin films synthesized at 1.05 slpm O_2 thermally treated to various temperatures.

3.3. Particle morphology and thin film formation

Figure 5 and **Figure 6** show micrographs of samples deposited at room temperature and then thermally treated to 160 °C and 350 °C. As-synthesized samples show a small amount of distinguishable particles embedded in a poorly crystalline matrix. Further increase in temperature triggers crystallization with the appearance of triangle-shaped, sharp-edged crystals with a wide size distribution ranging from a few hundred nanometres to a few micrometres. The sharp-edged geometry of the crystals implies that these can be attributed to the cuprite phase. Upon reaching a higher temperature, the most prominent crystals show spherical-like morphology, generally observed in systems where the dominant tenorite phase exists [24].

Furthermore, with the increase in temperature, the order of crystallinity visibly increases for both samples, and agglomeration occurs. However, generally one can observe that the film is non-uniform and that the particles are distinguishable from one another, exhibiting high apparent surface roughness. This is a consequence of the kinetic energy of particle impaction onto the substrate. Namely, this is a function of the pressure ratio between the reactor and the deposition chamber (p_1/p_2), which can be considered a power coefficient for the efficiency of the deposition; the bigger the difference, the higher the kinetic energy of the aerosol.

Critical kinetic energy must be reached for the particles to plastically deform onto the substrate, forming a dense nanoporous film. Otherwise, nanoparticles exhibit elastic behaviour and form a structure that can be considered more of a powder than a thin film. An aerosol influx of

10 slpm into the deposition chamber limits the minimum pressure in the chamber to ~200 Pa, which significantly reduces the power factor and deposition efficiency and affects the thin film formation. By reducing the nozzle size, a lower nominal aerosol flux can be used for deposition, lowering the minimum pressure limit by about two orders of magnitude (~2 Pa). As the power factor increases by roughly two orders of magnitude, so does the kinetic energy, which significantly shifts the morphology of the sample/thin film. This is best displayed in **Figure 7**, where in comparison to **Figure 5** and **Figure 6**, the film is uniform and shows porosity only on a meso-nanoscale. Moreover, no singular particles are formed on the surface, and the film appears to be of uniform phase.

For this investigation, copper oxide nanoparticles were synthesized, deposited onto a substrate and thermally treated to obtain a tenorite-dominated thin film at 350 °C. During the course of the study, appropriate chemical analysis was carried out on the plasma gas phase and on the synthesized materials.

Plasma diagnostic did not detect any difference in plasma composition with respect to the oxygen content in the gas mixture but rather the change in intensity. It was discovered that adding more oxygen results in less structurally organized material; yet, all of the samples crystallized equally in terms of temperature.

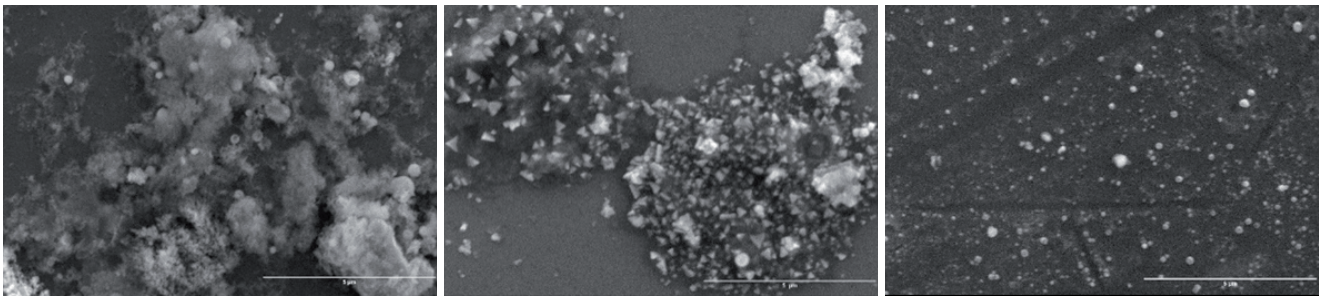

Figure 5. SEM micrographs of Cu_xO_y prepared with a mixture of 10 slpm nitrogen and 0.7 slpm oxygen (from left to right: 30 °C, 160 °C, 350 °C).

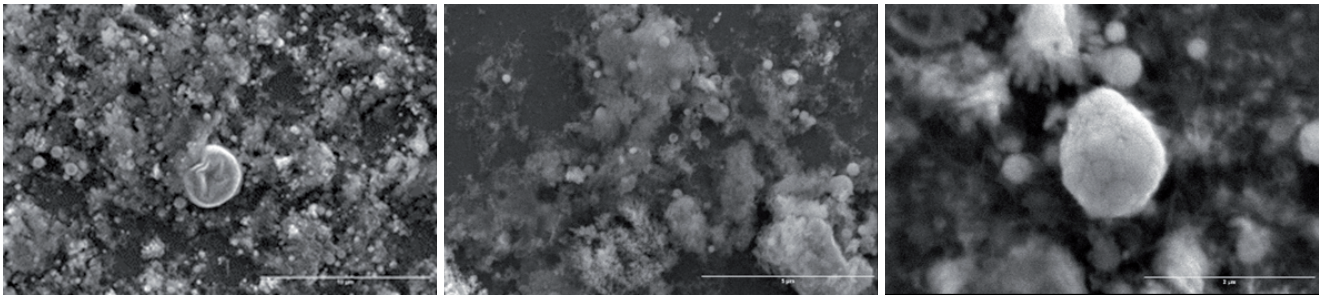

Figure 6. SEM micrographs of Cu_xO_y prepared with a mixture of 10 slpm nitrogen and 1.05 slpm oxygen (from left to right: 30 °C, 160 °C, 350 °C).

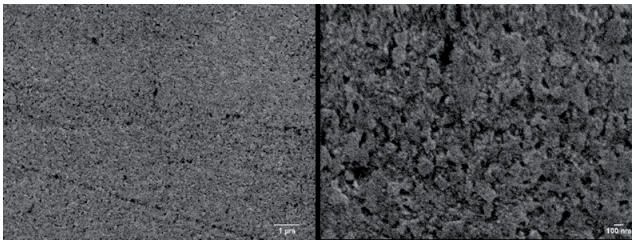

Figure 7. SEM micrographs of thin films of copper oxide nanoparticles deposited at 0.07 slpm O_2 and 1 slpm total flow through a smaller nozzle and lower chamber pressure (~2 Pa).

4. Conclusion

SPAD (Spark Plasma Ablation Deposition) setup can be used both as a nanoparticle synthesis method and as a nanoparticle deposition method. In any case, SPAD can produce lattice defects not only on the thin film's surface but also throughout the material.

To sum up, we demonstrate the ability to control the crystallinity range of synthesized materials through SPAD setup, through appropriate selection of ablation parameters (gas composition and flow) and post synthesis treatments.

5. References

[1] M. Nikzamir, A. Akbarzadeh, and Y. Panahi, "An overview on nanoparticles used in biomedicine and their cytotoxicity," *J. Drug Deliv. Sci. Technol.*, vol. 61, p. 102316, Feb. 2021

[2] A. Jurov *et al.*, "Atmospheric pressure plasma jet–assisted impregnation of gold nanoparticles into PVC polymer for various applications," *Int. J. Adv. Manuf. Technol.*, vol. 101, no. 1–4, pp. 927–938, Mar. 2019

[3] B. Farkaš and N. H. de Leeuw, "A Perspective on Modelling Metallic Magnetic Nanoparticles in Biomedicine: From Monometals to Nanoalloys and Ligand-Protected Particles," *Materials (Basel).*, vol. 14, no. 13, p. 3611, Jun. 2021

[4] J. Ma and S. Gao, "Plasmon-Induced Electron–Hole Separation at the Ag/TiO_2 (110) Interface," *ACS Nano*, vol. 13, no. 12, pp. 13658–13667, Dec. 2019

[5] T.-H. Lee, J. I. Gonzalez, J. Zheng, and R. M. Dickson, "Single-Molecule Optoelectronics," *Acc. Chem. Res.*, vol. 38, no. 7, pp. 534–541, Jul. 2005

[6] P. Matheu, S. H. Lim, D. Derkacs, C. McPheeters, and E. T. Yu, "Metal and dielectric nanoparticle scattering for improved optical absorption in photovoltaic devices," *Appl. Phys. Lett.*, vol. 93, no. 11, p. 113108, Sep. 2008

[7] H. A. Atwater and A. Polman, "Plasmonics for improved photovoltaic devices," *Nat. Mater.*, vol. 9, no. 3, pp. 205–213, Mar. 2010

[8] K. R. Catchpole and A. Polman, "Design principles for particle plasmon enhanced solar cells," *Appl. Phys. Lett.*, vol. 93, no. 19, p. 191113, Nov. 2008

[9] S. Pillai, K. R. Catchpole, T. Trupke, and M. A. Green, "Surface plasmon enhanced silicon solar cells," *J. Appl. Phys.*, vol. 101, no. 9, p. 093105, May 2007

[10] W. Kang, C. Cheng, Z. Li, Y. Feng, G. Shen, and X. Du, "Ultrafine Ag Nanoparticles as Active Catalyst for Electrocatalytic Hydrogen Production," *ChemCatChem*, vol. 11, no. 24, pp. 5976–5981, Dec. 2019

[11] C. Gao, F. Lyu, and Y. Yin, "Encapsulated Metal Nanoparticles for Catalysis," *Chem. Rev.*, vol. 121, no. 2, pp. 834–881, Jan. 2021

[12] X. Li, X. Hao, A. Abudula, and G. Guan, "Nanostructured catalysts for electrochemical water splitting: current state and prospects," *J. Mater. Chem. A*, vol. 4, no. 31, pp. 11973–12000, 2016

[13] T. V. Pfeiffer, J. Feng, and A. Schmidt-Ott, "New developments in spark production of nanoparticles," *Adv. Powder Technol.*, vol. 25, no. 1, pp. 56–70, 2014

[14] A. Voloshko and T. E. Itina, "Nanoparticle Formation by Laser Ablation and by Spark Discharges — Properties, Mechanisms, and Control Possibilities," *Nanoparticles Technol.*, pp. 1–12, 2015

[15] A. Schmidt-Ott, Ed., *Spark Ablation*, 1st ed. New York: Jenny Stanford Publishing, 2020.

[16] M. Stein and F. E. Kruis, "Scaling-up metal nanoparticle production by transferred arc discharge," *Adv. Powder Technol.*, vol. 29, no. 12, pp. 3138–3144, Dec. 2018

[17] J. Lu *et al.*, "Preparation of Ag nanoparticles by spark ablation in gas as catalysts for electrocatalytic hydrogen production," *RSC Adv.*, vol. 10, no. 63, pp. 38583–38587, 2020

[18] E. Hontañón *et al.*, "The transition from spark to arc discharge and its implications with respect to nanoparticle production," *J. Nanoparticle Res.*, vol. 15, no. 9, 2013

[19] M. Arreguín-Campos *et al.*, "Synthesis of paramelaconite nanoparticles by laser ablation," *J. Laser Appl.*, vol. 30, no. 1, p. 012012, 2018

[20] T. K. S. Wong, S. Zhuk, S. Masudy-Panah, and G. K. Dalapati, "Current status and future prospects of copper oxide heterojunction solar cells," *Materials (Basel).*, vol. 9, no. 4, pp. 1–21, 2016

[21] H. J. Song, M. H. Seo, K. W. Choi, M. S. Jo, J. Y. Yoo, and J. B. Yoon, "High-Performance Copper Oxide Visible-Light Photodetector via Grain-Structure Model," *Sci. Rep.*, vol. 9, no. 1, pp. 1–10, 2019

[22] S. Aghajani, A. Accardo, and M. Tichem, "Aerosol Direct Writing and Thermal Tuning of Copper Nanoparticle Patterns as Surface-Enhanced Raman Scattering Sensors," *ACS Appl. Nano Mater.*, vol. 3, no. 6, pp. 5665–5675, 2020

[23] S. Choudhary *et al.*, "Oxidation mechanism of thin Cu films: A gateway towards the formation of single oxide phase," *AIP Adv.*, vol. 8, no. 5, 2018

[24] Y. Alajlani *et al.*, "Characterisation of Cu_2O, Cu_4O_3, and CuO mixed phase thin films produced by microwave-activated reactive sputtering," *Vacuum*, vol. 144, pp. 217–228, 2017

Juraj Šipušić[1], Matej Ercegović[1], Filip Brleković[1]

Porosity of acoustic wood-wool cement board

[1]University of Zagreb, Faculty of Chemical Engineering and Technology, Marulićev trg 20, HR-10000 Zagreb, Croatia

Abstract

Wood-wool cement board (WWCB) is a porous composite material consisting of Portland cement inorganic binder mixed with wood-wool as reinforcement. It is widely used as thermal and acoustic insulator in buildings because of low density, high porosity, good fire resistance and compatibility with other binders and building materials. The majority of composite characteristics, including as density, strength, Young modulus, gas permeability, thermal conductivity, and thermal diffusivity, are dependent on porosity. Aside from density, the other qualities stated, including sound absorption coefficient, are affected by pore size distribution. The acoustic properties of air/WWCB interaction are described through air complex modulus and air complex effective density used in many acoustic models for porous materials. Two techniques for determining porosity are used and compared on samples of wood-wool cement board from normal manufacturing received from FRAGMAT H d.o.o. Sv. Križ Začretje, Croatia. The Archimedes technique is utilized to determine the real and apparent density of the bulk WWCB, while image analysis of the surface layer and deeper layers reached by grinding and polishing is used to analyze layer by layer porosity and pore size distribution. The approaches are compared based on their complexity, length of analysis, and the type and quality of information obtained.

***Keywords**: wood-wool cement board, porosity, image analysis.*

1. Introduction

1.1. Wood-wool cement composite boards

In 1880, a patent was filed in Germany describing the production of composite materials by binding wood wool with gypsum. At the beginning of the 20th century Sorel cement, based on magnesia, was used as binder for wood-wool. Due to the water solubility of gypsum and magnesia cement, improved wood-wool boards were manufactured by using Portland cement (PC) as a mineral binder. This type of composite material has been widely produced since the 1920s, and the term wood-wool cement board (WWCB) has been synonymous with it [1]. White Portland cement is used as a WWCB binder mostly for aesthetic purposes or when quick setting and hardening is required. Over time, the manufacturing process became increasingly automated, resulting in much larger production capacity; consequently, a contemporary facility with a dozen workers could easily create more than 100 m^3 of product per day. The wood used for the usual WWCB production in FRAGMAT H d.o.o., Sveti Križ Začretje, Croatia, is spruce and fir. Many types of wood are used worldwide, especially those with a lower content of soluble organic compounds that could delay the setting and hardening of Portland cement. Wood-wool is produced from air-dried (seasoned) tree trunks cut at 50 cm long logs. The shredding machine produces wood-wool of 1-5 mm width and 0.2-0.5 mm thickness. Acoustic insulation boards use finer wood-wool. WWCB properties are easily tunable during the production process. The range of product thickness varies usually between 25-100 mm .The desired density of WWCB can be achieved by adjusting porosity (mold thickness and cement and wood-wool dose), which typically varies from 150-700 kgm^{-3}. The use of a greater amount of cement binder poses the issue of a greater amount of heat emitted during exothermic hydration processes. Green WWCB are prepared and stacked in molds, where the typical maximum temperature rise attained in the stack is around 25-30 °C over an 8-24 h timeframe. In addition to the heat released during the curing and setting of PC the high alkalinity of the cement paste and humidity impair the strength and toughness of the wood-wool by partially depolymerizing cellulose fibers. Wood-wool includes a variety of complex chemical components and sugars that interfere with cement hydration processes and lower PC final strengths. Consequently, during regular production of WWCB some setting and hardening additives for Portland cement are used. The mechanical strength of WWCB depends on final porosity i.e. density. For insulation boards, it is in the range of 250-700 kgm^{-3}, with the denser product having better mechanical properties. The thermal conductivity [1] of dry WWCB increases with increasing final density, but is below 0.16 $Wm^{-1}K^{-1}$ and is comparable to the thermal conductivity of other building materials (wood, brick and concrete). However, the thermal conductivity is not the only important material property to make final comparisons/decisions, because the density, specific heat capacity, thermal diffusivity and thermal effusivity, porosity, water vapor permeability and water content during wetting/drying periods are also very important. The acoustic characteristics of WWCB are good, however the coefficient of sound absorption is frequency dependant owing to the complexity of acoustic wave (high frequency air pressure oscillations) porous material (WWCB) interaction [2-6]. Fur-thermore, the specific method of acoustic WWCB appli-cation, such as directly on the thick wall or with an air gap, results in significantly varied sound absorption capabilities [1,7]. Not only the density of the WWCB material, i.e. the porosity, but also the thickness, permeability and pore tortuosity have a significant influence on the sound absorption coefficient.

1.2. Theoretical background about sound propagation

By definition, sound wave is a wave of compression and rarefaction, by which sound is propagated in an elastic medium such as air. Sound energy balance is given by Eq. (1). Incident sound wave has incidence energy Einc and after hitting the wall (WWCB), energy can be divided into three components, as shown in Fig 1. One portion of the energy is reflected back (Eref), while another portion (Etran) is able to transmit through the material. Eabs represents the part of the absorbed sound energy which is converted into heat due to the internal friction and viscoelastic effects.

$$E_{inc} = E_{ref} + E_{abs} + E_{tran} \quad (1)$$

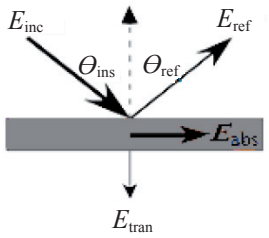

Fig. 1. Sound energy balance on the phase boundary [8, 9].

It is worth noting that in general, acoustic wave impignes the boundary at an angle θ_{ins}.

1.3. Methods for measuring sound absorption coefficient

Generally sound absorption coefficient is adopted as the index for evaluating the sound absorbing performances of a material [8,9]. The effectiveness of a sound absorber is quantified by the absorption coefficient Eq. (2), which defines the part of acoustical energy of the incident wave that is actually absorbed by the material.

$$\alpha = E_{abs} / E_{inc} \quad (2)$$

The part of sound wave which is transferred to the material enters its pores and a certain amount of its energy is converted into heat because of the friction and the viscosity resistance between the air molecules and the wall of pores. In this way, the sound energy is absorbed [5, 6, 9]. Sound absorption coefficient is measured using different measuring techniques, each with its own advantages and limitations. Standard techniques for measuring sound absorption coefficient are reverberation room (random incidence sound wave) and impedance tube (normal incidence sound wave only). Reverberation room tech-nique is used for measuring diffuse absorption sound coefficient

in diffuse sound field i.e. in similar conditions as occur in practice. This method examines sound decay time needed for incident sound pressure to reduce for 60 dB. Reverberation room method is based on the Sabine formula [10] given by Eq. (3):

$$T = 0{,}05V / aS \tag{3}$$

where:

V – volume of the room (m^3)

a – average absorption coefficient

S – area of sample material (m^2)

The method requires a large sample area and a large volume of reverberation room and it is suited for investigating the sound absorption of massive building materials such as plaster boards, concrete and wood composite materials.

The sound absorption coefficient of an acoustic material at normal incidence is measured using the impedance tube method, since only a standing wave at normal incidence is maintained during the measurement. The impedance tube is generally used to measure the sound absorption of small samples on a laboratory scale, usually with a diameter of 30 or 40 mm. Two methods are generally used to measure the sound absorption coefficient at normal incidence for small samples: the standing wave ratio method (ISO 10534-1 standard), and the transfer-function method, standardized by ISO 10534-2. The usual outline of an impedance tube is shown in the Fig 2.

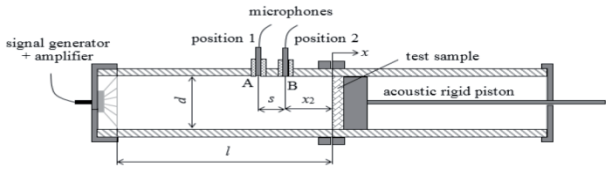

Fig. 2. Standard impedance tube [11]

A loudspeaker is frequently used as a sound source, microphones monitor dynamic pressure oscillations at various points in the tube, and the test sample is connected with a moveable acoustically rigid piston. Microphone signals are frequently amplified, filtered and recorded by PC software.

1.4. WWCB as porous sound absorber material

WWCB boards act as acoustic absorbers due to their high porosity. The incoming sound wave periodically forces the air in the porous structure of the material, where the sound energy is lost through viscoelastic effects and friction with the pore wall. The vibration of the air in the open pores dissipates the mechanical energy in the form of heat. The main acoustic characteristic of WWCB (Fig. 3) is strong sound absorption in the higher frequency range (1000-4000 Hz) due to the open porosity of the WWCB. Also the morphology of the pores and their size contribute to sound absorption at higher frequencies. At lower frequencies (<1000 Hz) the sound is poorly ab-sorbed in the material due to a large difference between the sound wavelength and material thickness. Other acoustic materials used in construction exhibit comparable properties.

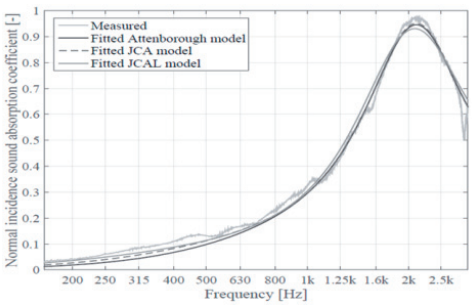

Fig. 3. Characteristic sound absorption coefficient for WWCB [7]

Acoustic models used [2-6] describe the interaction of acoustic wave/porous materials where the effect of vibration of the material frame is excluded. Those models are able to predict energy dissipated by the air that vibrates inside the pores.The frequently applied models are Delany-Bazley-Miki [2], Zwikker and Kosten [3], Attenborough [4], Johnson-Champoux-Allard (JCA) [5] and Johnson-Champoux-Allard-Lafarge [6] (JCAL) model. Delany-Bazley-Miki model describes sound wave propagation in fibrous materials. This model is simple and it has only one parameter, flow resistivity (σ/Pasm^{-4}). Zwikker and Kosten describe sound propagation in cylindrical pores of porous materials. The equation of Zwikker and Kosten in Eq. (12) is analogous to the Helmholtz equation, which describes sound propagation in free air without dissipation. .Because of porosity, the effective density and effective bulk modulus of air are complex functions of the frequency and material morphology:

$$\nabla p + \omega^2 \frac{\rho_{eq}}{K_{eq}} p = 0 \tag{12}$$

where p is the acoustic pressure (Pa), ω the angular frequency (s^{-1}), ρ_{eq} is the effective density (kgm^{-3}) and K_{eq} is the effective bulk modulus ($kgm^{-1}s^{-2}$). Attenborough [4] model includes four parameters; porosity, tortuosity, flow resistivity and pore shape factor. This model is best suited for granular materials as soils, sands and resin-bonded materials. Tortuosity is one important parameter which is related to the curvature of the pore path through the material [12, 13] The Johnson-Champoux-Allard [5] model has five parameters: porosity, flow resistivity, tortuosity, viscous characteristic length and thermal characteristic length. Only porosity and flow resistivity values are often not fitted but rather obtained by independent measurement. There are two new physical parameters which have been considered in the model: viscous characteristic length and thermal characteristic length, which are related to microstructure of the pores. It is worth mentioning Wilson model [14, 15] that uses viscous and thermal characteristic length for empirical modeling of acoustic materials. Effective density (ρ_{ef}) and bulk modulus (K_e) in JCA model [5] are given by equations (13) and (14).

$$\rho_e(\omega) = \frac{\alpha_\infty \rho_0}{\phi}\left(1 + \frac{\sigma\phi}{i\omega\rho_0\alpha_\infty}\sqrt{1 + \frac{4i\alpha_\infty^2\eta\rho_0\omega}{\sigma^2\Lambda^2\phi^2}}\right) \tag{13}$$

$$K_e(\omega) = \frac{\frac{\gamma P_0}{\phi}}{\gamma-(\gamma-1)/\left(1+\frac{8\eta}{i\rho_0\omega N_{pr}\Lambda'^2}\sqrt{1+\frac{i\rho_0 N_{pr}\Lambda'^2}{16\eta}}\right)} \quad (14)$$

where:

d – thickness of the sample (m)

ρ_0 – air density (kg m^{-3})

c_0 – speed of sound in air(m s^{-1})

α_∞ – tortuosity

σ – airflow resistivity (Pa s m^{-4})

φ – porosity

ω – angular frequency (s^{-1})

η – dynamic viscosity of air (Poiseuille) (1.84x10^{-5} Pa s at 20 °C)

Λ – viscous characteristic dimension (m) (range 10-1000 μm)

Λ' – thermal characteristic dimension (m) (range 10-1000 μm)

p_0 – atmospheric pressure (Pa)

γ – specific heat ratio (adiabatic exponent) equals 1.40 for air

N_{Pr} – Prandtl number (for air at 20 °C equals 0.71)

JCA is one of the most widely used in acoustic engineering for porous materials nowadays. Botterman [7] shows acceptable agreement between theoretical and measured values of sound absorption coefficient for WWCB. Because closed pores do not contribute to sound absorption, open porosity, accessible to air passage, is one of the most essential elements of an acoustic model. Pore size distribution must be considered for porous materials because some pores are too small and others are too big for efficient dampening of sound wave energy.

1.5. Method for measuring porosity of building materials

The porosity of building materials such as WWCB can be considered as macro porosity. It contains a lot of voids, cavities and interconnected pores which are not straight and neither cylindrical. There are many methods for measuring porosity of bulk materials like helium pycnometer, computed tomography (CT) [16] or by digital image analysis [17]. As previously mentioned, pores in materials can be closed or open. Closed pores have an influence on physical properties of a material such as bulk density, mechanical strength and thermal conductivity but they are not acoustically effective. On the other hand, open pores are interconnected inside the material which is effective for damping sound wave energy.

2. Experimental procedure

Two wood-wool cement boards from regular production obtained from FRAGMAT H d.o.o. Sv. Križ Začretje, Croatia, were used for the purposes of this work. Boards were 2.5 cm and 1.0 cm thick. The surface layer and the deeper layers of WWCB, which are accessible by grinding and polishing, are used for the layer-by-layer determination of the porosity by image analysis. The main goal of the research was to discover correlations between different methods of measuring density. Three different methods were used in this work: theoretical density calculation method, Archimedes method and digital image analysis. The methods are compared in terms of complexity, duration of analysis and type and quality of the information obtained.

2.1. WWCB density calculation method

WWCB is a material which consists of Portland cement, wood-wool (spruce) and water. The standard WWCB has about 20-25 mass percent wood wool in the material. If the mass fractions of three main components of WWCB are known, it is possible to calculate theoretical density of the composite material for different porosities. Eq. (15) defines density with 0% porosity as follows:

$$\rho_0 = \frac{\sum m}{\sum V} = \frac{m_{ww}+m_{cem}+m_{wat}}{\frac{m_{ww}}{\rho_{ww}}+\frac{m_{cem}}{\rho_{cem}}+\frac{m_{wat}}{\rho_{wat}}} \quad (15)$$

where:

m_{ww} – mass of wood-wool (g)

m_{cem} – mass of cement (g)

m_{wat} – mass of water (g)

ρ_{ww} – density of dry wood-wool; 0,421 g cm^{-3}

ρ_{cem} – density of cement; 3,00 g cm^{-3}

ρ_{wat} – density of water; 0,997 g cm^{-3}

The calculation of the WWCB density with different composition is given in Table 1. Due to the comparison with WWCB from the manufacturer, mass fractions of wood-wool employed in calculations are taken in a tight range. The calculation is for wet WWCB from production (w/c=0,45). Water is consumed in excess (more than is required for complete theoretical hydration) of cement). The density of porous solids depends on porosity according to the Eq. (16):

$$\rho_{apparent} = \rho_0(1-P) \quad (16)$$

where P is porosity (total pore volume divided by total solid volume), ρ_0 is true density of material under study (kg m-3) and ρapparent is apparent solid density (kg m-3) taking also pore volume into account.

Table 1. Calculated theoretical density of wet WWCB. Porosity varies from 50 to 70%.

$w_{wood\,wool}$	$w_{cem-water}$	w/c	w_{cem}	w_{wat}	ρ_0	P=50%	P=55%	P=60%	P=65%	P=70%
0	1		0,690	0,310	1,848	0,924	0,832	0,739	0,647	0,554
0,15	0,85		0,586	0,264	1,225	0,613	0,551	0,490	0,429	0,368
0,2	0,8		0,552	0,248	1,101	0,551	0,496	0,441	0,385	0,330
0,25	0,75		0,517	0,233	1,000	0,500	0,450	0,400	0,350	0,300
0,3	0,7		0,483	0,217	0,916	0,458	0,412	0,367	0,321	0,275
0,35	0,65	0,45	0,448	0,202	0,845	0,423	0,380	0,338	0,296	0,254
0,4	0,6		0,414	0,186	0,784	0,392	0,353	0,314	0,275	0,235
0,45	0,55		0,379	0,171	0,732	0,366	0,329	0,293	0,256	0,220
0,5	0,5		0,345	0,155	0,686	0,343	0,309	0,274	0,240	0,206
0,55	0,45		0,310	0,140	0,645	0,323	0,290	0,258	0,226	0,194
0,6	0,4		0,276	0,124	0,609	0,305	0,274	0,244	0,213	0,183

where $w_{wood\text{-}wool}$ is mass fraction of wood-wool, $w_{cem+water}$ mass fraction of cement paste; w/c water/cement factor, w_{cem} and w_{wat} mass fraction of cement and water for given w/c factor, ρ_0 density of WWCB with 0% of porosity, P (50-70%) density for given porosity of WWCB

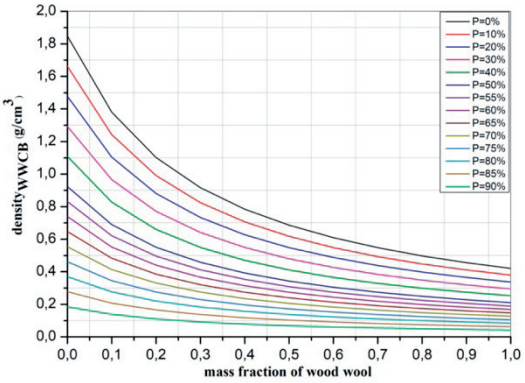

Fig. 4. Calculated density of WWCB for a wider range of mass fraction of wool wool

The calculation method is also carried out for the dry WWCB, whereby a w/c ratio of 0.24 is theoretically required for the complete hydration of Portland cement. The density of WWCB with changing porosity is given in Table 2.

Table 2. Calculated theoretical density of dry WWCB. Porosity varies from 50 to 70%.

$w_{wood\,wool}$	$w_{cem-water}$	w/c	w_{cem}	w_{wat}	ρ_0	P=50%	P=55%	P=60%	P=65%	P=70%
0	1		0,806	0,194	2,160	1,080	0,972	0,864	0,756	0,648
0,15	0,85		0,685	0,165	1,334	0,667	0,600	0,533	0,467	0,400
0,2	0,8		0,645	0,155	1,183	0,591	0,532	0,473	0,414	0,355
0,25	0,75		0,605	0,145	1,063	0,531	0,478	0,425	0,372	0,319
0,3	0,7		0,565	0,135	0,965	0,482	0,434	0,386	0,338	0,289
0,35	0,65	0,24	0,524	0,126	0,883	0,442	0,397	0,353	0,309	0,265
0,4	0,6		0,484	0,116	0,814	0,407	0,366	0,326	0,285	0,244
0,45	0,55		0,444	0,106	0,756	0,378	0,340	0,302	0,264	0,227
0,5	0,5		0,403	0,097	0,705	0,352	0,317	0,282	0,247	0,211
0,55	0,45		0,363	0,087	0,660	0,330	0,297	0,264	0,231	0,198
0,6	0,4		0,323	0,077	0,621	0,310	0,279	0,248	0,217	0,186

2.2. Digital image analysis

This paper introduces a novel approach for determining the porosity of WWCB. Image analysis is a simple, low-cost, and straightforward approach for measuring the porosity of various materials, including WWCB. A freeware programme such as ImageJ© enables simple image processing, e.g. calculating the percentage of pixels of a certain red-blue-green component (RGB). On this basis, the contrasts in the picture may be distinguished and, finally, it is possible to determine which portion of the pixels belongs to the material and which part is associated with the pores of WWCB. The samples were prepared by coloring the surface of WWCB material with a thin film of white color to increase the contrast between the surfaces and pores of the material. Subsequently, such prepared samples were scanned and the image was refined using ImageJ© to determine the ratio of white surface pixels and darker pixels representing the pores. In the next step the surface of the composite was polished in an equal layer, with 0.5 to 1 mm of surface material removed. This process was repeated 25 times to establish the porosity of the composite board through its cross section.

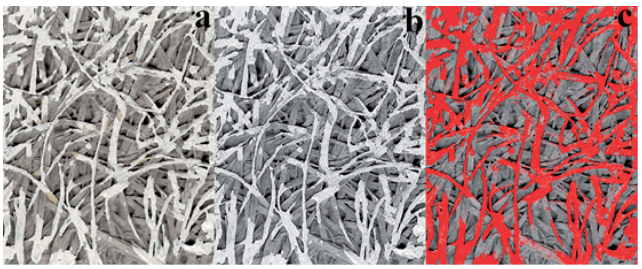

Fig. 5. Example of scanned image treatment in ImageJ. Colored and scanned composite board (a), scanned image transformed to 8 bit image (b) and processed image with already determined surface pixels (c).

2.3. Archimedes method

Archimedes method is applied for true and apparent density determination of the bulk WWCB. Fluids (liq-uids and gasses) in the gravity filed exert buoyancy on the immersed objects. The net buoyancy force is di-rected upward (opposite of the body weight) according to the following formula:

$$F_{buoyancy} = V_{body} \cdot \rho_{fluid} \cdot g \qquad (17)$$

where V_{body} is immersed body volume (m^3), ρfluid is fluid density (kg m^{-3}) and g is the local gravity acceleration, around 9.81 m s^{-2} at 45° latitude. The Archimedes method of density determination is routinely performed in many laboratories for unknown liquid or solid density measurement. The simple measurement setup could be bought with a laboratory scale/balance.

The ambient temperature should be steady, all elements of the apparatus and the sample should be at the same temperature, and there should be no vibrations or air turbulence for optimal stability and precision. However, one should take into account that if the mass of the solid sample is weighted in air, a correction for air buoyancy (i.e. air density) must be performed.

The open pores are accessible to the fluid, and could be fully saturated with a measuring fluid, while closed pores are not accessible to the fluid, and the sample is usually broken into fine powder thus effectively break-ing all closed pore spaces and making true solid density determination possible. If the solid density is larger than the liquid density, sample density may be calculated by simply weighing the sample in air and submerged in fluid.

However, if the apparent solid density is less than the fluid density, the sample must be forced below the fluid surface. This applies to WWCB (wood-wool cement board) samples with porosities greater than 50%. The WWCB sample for the determination of the apparent density (the penetration of liquid into the pore space must be avoided) is prepared by placing the sample in plastic vacuum bags and sealing the bag. Now, the correction for the immersed plastic bag and solid shaft volume should be made in order to make apparent density measurement. Measuring the actual density of WWCB (the average density of spruce wood and hydrated cement) is relatively easy, as the sample is slightly saturated with the liquid (the open porosity consists of large pores).

3. Results and discussion

3.1. Archimedes method
(calculation for WWCB without pores)

m_{WWCB}=69.69 g

m_{d0} =55.50 g

$\rho_{H2O(25°C)}$=0.997gcm^{-3}

V_{d0}=55.50 g / 0.998 g cm^{-3}=55.67 cm^3

ρ_{WWCB}= 69.69 g / 55.67 cm^3 =1.252 g cm^{-3}

3.2. Archimedes method
(calculation for WWCB with pores)

m_{WWCB}= 69.69 g

V_{d1}= 162.65 cm^3

after making correction for plastic bag and solid shaft:

V_{d2}= 155.93 cm^3

ρ_{WWCB}= 69.69 g / 155.93 cm^3 = 0.447 g cm^{-3} (WWCB with pores)

3.3. Porosity calculation for WWCB (2.5 cm thick)

From Eq. (16): 1-P=ρ/ρ_0

P=64,3%

m_{WWCB} - is mass of WWCB (g), m_{d0} - mass of displaced water for WWCB (g), V_{d0} – volume of displaced water for WWCB (cm^3), ρ_{WWCB} – density of WWCB (g cm^{-3}), $\rho_{H2O(25°C)}$ – density of water (g cm^{-3}), V_{d1} - volume of displaced water due to WWCB, plastic bag and solid shaft (g cm^{-3}), V_{d2} - volume of displaced water due to WWCB after correction (cm^3)

3.4. Digital image analysis results

The "wall effect" in the WWCB was revealed in the first results of digital image analysis. The first layer scanned had a higher porosity (70.06%) than the subsequent layer after the first polishing of the board (64.37%). Fig 6. shows the “wall effect” and the difference between the porosities of these two layers.

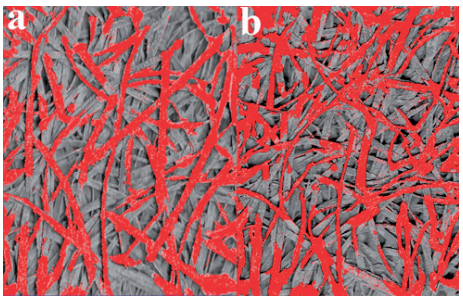

Fig. 6. Difference between the first layer with the “wall effect” (a) and the second layer with 1 mm of material removed (b)

Figure 7 depicts the determined porosity values through the cross section, with the average porosity including and omitting the less porous initial layer. The average porosity of 25 layers including the first layer is 64.19 % and the determined porosity without the "wall effect" is 63.94 %.

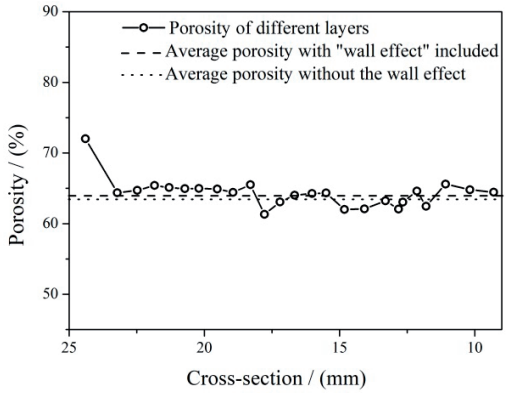

Fig. 7. Graphical representation of porosity throughout the WWCB and average porosities

4. Conclusion

Wood-wool cement board is a lightweight building material used for thermal and acoustic insulation of buildings. The inorganic binder Portland cement contributes to the mechanical strength of the composite while wood-wool contributes to the toughness of the composite. Lower density (more porosity) board has lower thermal conductivity but also worse mechanical properties. The acoustic properties of WWCB depend on the complex interaction between sound waves and porous material, and not only the total porosity but also the pore size distribution and the tortuosity of the pores influence the frequency-dependent sound absorption. Lower frequencies are less attenuated, therefore work is being done to enhance sound attenuation of WWCB at lower frequencies by surface texturing and extra acoustic material sandwiching.

The method of theoretically calculating the porosity of WWCB as a function of raw material composition is satisfactory, but it does not provide details of the pore space as obtained from digital image analysis of the polished surfaces, nor of the porosity gradient observed near the board surface. This phenomenon is explained by the “wall effect”, similar to the packing density of granular materials near the walls of the container. The original and actual

WWCB density can be determined by the Archimedes method, and the calculated porosity agrees with the results of digital image analysis. This method is cost-effective. However, it necessitates the preparation of numerous polished surfaces in order to maintain the integrity of the pores, which renders this method laborious. The use of computational tomography measurements has the potential to reduce this burden and provide a de-tailed pore structure; however, this may incur a high cost and result in a low sample rate.

5. Acknowledgment

This work is part of scientific investigations financed through the project "Acoustical incombustible plate" KK.011.1.02.0299.

6. References

[1] https://portal.research.lu.se/en/publications/woodwool-slabs-production-properties-and-use (20.02.2023.)

[2] Miki, Y. Acoustical properties of porous materials - Modifications of Delany-Bazley models. J. Acoust. Soc. Jap. 11 (1990). 19-24

[3] Zwikker, C.,Kosten, C.W. Sound absorbing materials, Elsevier, USA, (1949)

[4] Attenborough, K. Acoustical characteristics of rigid fibrous absorbents and granular materials. J. Acoust. Soc. Am. 73 (1983) 785-799

[5] Champoux, Y., Allard, J.F. Dynamic tortuosity and bulk modulus in air-saturated porous media. J. Phys. 70 1975-1979, (1991)

[6] Lafarge D., Lemarinier P., Allard J.-F., Tarnow V. Dynamic compressibility of air in porous structures at audible frequencies. J. Acoust. Soc. Am. 102 (1997) 1995-2006

[7] Botterman, B., WWCB characterizing, modelling and optimizing the sound absorption of wood-wool cement boards. Master Thesis (in English), Eindhoven, 2016

[8] Desideri U., Asdrubali F. Building Envelope In: Desideri U., Asdrubali F. (eds) Handbook of Energy Efficiency in Buildings A Life Cycle Approach. Elsevier, USA, 2019, pp. 295-439.

[9] Fabiani, C., Pisello, A. L., Paksoy, H. Novel Building Materials. In: Dincer I. (eds) Comprehensive Energy Systems. Elsevier, Netherlands, 2018 pp. 980–1017

[10] EN ISO 354: Acoustics – Measurement of sound absorption in a reverberation room. 2003-12

[11] Koruk H. An assessment on the performance of impedance tube method. Noise Control Eng. J. 62 (2014), 264-274

[12] Jinlong F., Hywel R. T., Chenfeng L. Tortuosity of porous media: Image analysis and physical simulation. Earth-Sci. Rev. 212 (2021) 103439

[13] Johnson, D. L., Koplik, J., Dashen, R. Theory of dynamic permeability and tortuosity in fluid-saturated porous media. J. Fluid Mech. 176 (1987) 379–402

[14] Wilson, D. K. Simple, Relaxational Models for the Acoustical Properties of Porous Media. Appl. Acoust. 50 (1997) 171 -188

[15] Wilson, D. K. Relaxation-matched modeling of propagation through porous media, including fractal pore structure. J. Acoust. Soc. Am. 94 (1993) 1136–1145

[16] Reedy, C.L., Reedy, C.L. High-resolution micro-CT with 3D image analysis for porosity characterization of historic bricks. Herit. Sci. 10 (2022) 1–22

[17] Songsong, L., Tao, M., Hongqi, S., Zhongjia, W., Jiabin L. Relationship between percolation mechanism and pore characteristics of recycled permeable bricks based on X-ray computed tomography. Rev. Adv. Mater. Sci. 60 (2021) 207–215

Engineering Power – Bulletin of the Croatian Academy of Engineering Vol. 17(4) 2022 – ISSN 1331-7210
Publisher: Croatian Academy of Engineering (HATZ), 28 Kačić Street, P.O. Box 14, HR-10105 Zagreb, Republic of Croatia
Editor-in-Chief: Prof. Vedran Mornar, Ph.D., President of the Academy
University of Zagreb, Faculty of Electrical Engineering and Computing
Editor: Prof. Bruno Zelić, Ph.D., Vice-President of the Academy
University of Zagreb, Faculty of Chemical Engineering and Technology
Guest-Editor: Prof. Stanislav Kurajica, Ph.D., University of Zagreb, Faculty of Chemical Engineering and Technology
Activities Editor: Tanja Miškić Rogić
Editorial Board: Prof. Vedran Mornar, Ph.D., Prof. Vladimir Andročec, Ph.D., Prof. Bruno Zelić, Ph.D., Prof. Vladimir Mrša Ph.D., Prof. Neven Duić, Ph.D.
Editorial Board Address: Croatian Academy of Engineering (HATZ), "Engineering Power" – Bulletin of the Croatian Academy of Engineering, Editorial Board, 28 Kačić Street, P.O. Box 59, HR-10001 Zagreb, Republic of Croatia
E-mail: hatz@hatz.hr
Graphical and Technical Editor: Tiskara Zelina, Ltd., Zelina
Proof-reader: Miroslav Horvatić, MA
Press: Tiskara Zelina, Ltd., Zelina
Circulation: 250